International Journal of Coal Science & Technology (2025) 12:5
https://doi.org/10.1007/s40789-024-00739-0

RESEARCH

Quantitative characterization of the multiscale mechanical properties of low-permeability sandstone roofs of coal seams based on nanoindentation and triaxial tests and its implications for CO_2 geological sequestration

Feng Cao[1] · Jianhua He[1,2] · Hongxiu Cao[1] · Hucheng Deng[1,2] · Andrew D. La Croix[3] · Rui Jiang[1] · Ruixue Li[1,2] · Jiarun Li[4]

Received: 1 July 2024 / Revised: 16 September 2024 / Accepted: 9 November 2024

Abstract

Microstructural heterogeneity of low-permeability sandstone roofs of deep unmineable coal seams due to diagenesis significantly affects rock mechanical behavior, greatly impacting the sealing potential of in situ CO_2 sequestration and the structural stability of the geological formation. However, little is known about how the microstructure of different mineral groups influences the multiscale mechanical behavior of deep sandstone. This study proposes a new method for quantitatively characterizing the multiscale mechanical properties of low-permeability sandstone and shows the mechanisms responsible for mechanical failure at the micro-, meso-, and macroscale. Triaxial compression tests and targeted nanoindentation tests were conducted to assess the micro- and macroscale mechanical properties of different types of sandstone. The micro- and macroscale experiments were coupled with numerical simulations of compression using a unified cohesive model based on Voronoi polygons to clarify the multiscale mechanical behavior. The results indicate that quartz, the primary mineral component of the sandstones examined, exhibits the strongest micromechanical properties, followed by feldspar, calcite, and clay minerals. Compared to polycrystalline quartz, monocrystalline quartz has a more stable microstructure and is mechanically stronger. The macro-mechanical properties of tight sandstone samples are weakened by increased microstructural inhomogeneity and larger grain size. This leads to a higher likelihood of splitting damage, characterized by a high degree of discrete and weak stress sensitivity. The major conclusion is that the positive rhythm lithofacies of medium-grained sandstone to siltstone are the most favorable for efficient CO_2 sequestration in deep unmineable coal seams.

Highlights

- The micromechanical properties of common minerals and their main influencing factors in tight sandstone roofs of coal seams are demonstrated for the first time
- A quantitative method for characterizing the multiscale mechanical properties of tight sandstone has been developed, and the feasibility of rapidly evaluating the macromechanical properties of arbitrary-shaped rocks in deep earth engineering has also been verified
- The effects of grain size and fabric on the macroscopic and micro-mechanical properties and fracture mechanical behaviors of tight sandstone are showcased

---

✉ Jianhua He
hejianhuadizhi@163.com

[1] College of Energy, Chengdu University of Technology, Chengdu 610059, China

[2] State Key Laboratory of Oil and Gas Reservoir Geology and Exploitation, Chengdu University of Technology, Chengdu 610059, Sichuan, China

[3] Sedimentary Environments and Analogues Research Group, School of Science, University of Waikato, Hamilton 3240, New Zealand

[4] College of Petroleum Engineering, Liaoning Petrochemical University, Fushun 113001, China

Keywords Low-permeability sandstone roofs of coal seams · Triaxial test · Nanoindentation test · Mechanical properties · Fracture mechanical behavior · CO_2 sequestration

1 Introduction

China possesses abundant coal resources, including a significant number of unmineable coal seams. These deep unmineable coal seams exhibit considerable potential for CO_2 sequestration, primarily attributed to their distinctive reservoir physical properties and high adsorption capacity for CO_2 (Gale and Freund 2001; Pan et al. 2017). Nevertheless, the injection of CO_2 into the coal seam might induce differential expansion due to the adsorption of both CO_2 and CH_4 by the coal. This phenomenon could potentially destabilize the geological structure, thereby triggering coal rock rupture and subsequently causing the upward release of CO_2 (Rutqvist et al. 2008). The roof of the upper section deep coal seam commonly consists of low-permeability (i.e., "tight") sandstones or other low-permeability rock layers. These formations can serve as a reservoir to capture the upward migrating CO_2 from the coal seams and act as a protective barrier to prevent additional CO_2 leakage into shallower strata (Zhou et al. 2021; Liu et al. 2022). However, there are gaps in knowledge about the macroscopic-microscopic mechanical properties and damage characteristics of deep coal seam roofs, which need to be addressed to evaluate their potential for CO_2 sequestration and to reduce geologic hazards, including groundwater contamination, disruption of underground ecosystems, and surface uplift resulting from CO_2 leakage (Zhang et al. 2021; Li et al. 2024). Hence, it is crucial to investigate the mechanical characteristics of tight sandstone roofs of deep coal seams for deep energy exploration, development, and geological carbon sequestration.

To date, there are two main methods for the quantitative characterization of tight sandstone mechanical properties, namely, (1) obtaining static parameters through testing, and (2) calculating continuous rock mechanical parameters using well-logging data. The most prevalent testing method is the traditional triaxial test. While this approach has several drawbacks, including a prolonged testing duration, high costs, and the requirement for destructive utilization of core material. (Sone and Zoback 2014; Jia et al. 2018; Luo et al. 2020). However, calculations from well-loging curves are also affected by various factors, such as wellbore quality and associated drilling fluid characteristics, which can result in large errors in the calculation of the mechanical properties of the rock (Kneuker et al. 2017). Significantly, both methods are only able to obtain macroscopic mechanical parameters because they cannot be implemented to quantitatively analyze the micromechanical properties of various mineral in rock. But macroscopic damage is often controlled by microscopic cracks within the mineral grains that constitute the sedimentary rocks (Xu et al. 2021). The microstructure of sandstone, also known as the fabric or internal structure, is a manifestation of the mineral grain structure and arrangement structure and includes attributes such as grain morphology, continuity, geometry, composition, grain size change, degree of crystallization and interfacial contact (Spangenberg 1998; Liang et al. 2021). In addition, sandstone often contains a variety of minerals with different physical and mechanical properties and geometric forms. Moreover, many pores, defects, and microcracks are present inside sandstone, forming a very nonuniform (heterogeneous) microscopic fabric. Therefore, the microstructure of sandstone significantly impacts its macroscopic strength and failure mechanical behavior. Due to the heterogeneity in geometric structure, physical and mechanical properties, and arrangement of mineral grains, under the same external force, different mineral fabrics of sandstone are anisotropic in terms of microscopic grain deformation and load-bearing properties, leading to differences in the propagation and extension of microcracks (Guo et al. 2021; Huang et al. 2022). However, few studies have investigated the effects of differences in mineral grain fabric on the macromechanical and micromechanical properties of tight sandstone. There is a large research gap related to how these differences in micromechanical properties affect the behavior of sandstone specimens undergoing micromechanical damage until macromechanical fracturing occurs.

Nanoindentation testing is a material mechanical testing method that has developed rapidly in recent years. This technique is increasingly being applied in the characterization of the micromechanical properties of rock materials (Ma 2020). Nanoindentation testing has the advantage of easy sampling ability, a short testing time, single sample test repeatability, and test data reliability. Moreover, this testing method compensates for the difficulty in obtaining the mechanical properties of rocks and minerals at the micro/nano-scale through macroscopic tests (Magnenet et al. 2011; Abedi et al. 2016). Recently, two main types of research methods for evaluating multiscale mechanical properties based on nanoindentation testing have been described. The first type of method involves the use of a grid lattice nanoindentation test combined with a statistical deconvolution technique to perform statistical characterization of the areal mechanical properties of the material (Sun et al. 2020a; Li et al. 2021a; Ma et al. 2022). Cong et al. (2023) conducted a quantitative analysis of the mechanical responses and indentation patterns of minerals across various sandstone formations through grid nanoindentation tests and performed a comparative study of the results. Li et al. (2021b) used three different deconvolution techniques—the probability density function (PDF), cumulative distribution function (CDF) and Gaussian mixture model (GMM)—to perform cross-scale mechanical characterization of two types of sandstone lithofacies based on big data statistics and carried out statistical analysis. The deconvolution technique and the upscaling model were evaluated. Manjunath et al. (2019) utilized the deconvolution of the probability density function for all indentation moduli and hardness values to determine the three-phase structure of Gondwana coal, specifically distinguishing between quartz, organic matter, and kaolinite. Furthermore, they employed an energy model to calculate the fracture energy release rate at specific pop-in event points on the *P–h* curve, thereby providing validation for their microscopic fracture toughness model. The second type of method consists of targeted nanoindentation tests that combine scanning electron microscopy (SEM), backscatter electron diffraction (BSE), energy dispersive X-ray fluorescence spectroscopy (EDS), X-ray diffraction (XRD), and computed tomography (CT) to accurately measure the micromechanical parameters of a single mineral phase (Du et al. 2020; Cheng et al. 2022; Abdallah et al. 2023; Tang et al. 2022). Sun et al. (2021) identified and positioned sandstone mineral components through XRD, SEM and EDS and conducted targeted nanoindentation tests to determine the mesoscale rheological characteristics of minerals. Zheng et al. (2023) investigated the relationship between the macroscopic and microscopic friction coefficients of sandstone structural surfaces based on targeted nanoindentation tests and direct shear tests. Nie et al. (2024) scaled up the mechanical parameters and discovered that an increase in non-homogeneity and the presence of hard minerals could enhance the accuracy of the scaled-up results from 50 coal samples. Kossovich et al. (2016) analyzed the modulus of elasticity and hardness for both vitrinite and inertinite in coal-rock across various orientations. Utilizing targeted nanoindentation experiments, they discovered that the mechanical strength of the micro-components is obviously greater when measured parallel to the laminae. This observation further indicates the existence of microscopic inhomogeneity within the coal-rock structure. Currently, most research concerning the micromechanical properties of coal rocks and sandstones through nanoindentation is confined to the measurement and statistical analysis of mechanical parameters, including hardness and modulus of elasticity. However, the in-situ stress response and corresponding microscopic fracture modes of a single mineral phase in tight sandstone are still not fully understood. In addition, studies on the distribution characteristics of sample data on micromechanical parameters are lacking. Moreover, deep underground rocks are susceptible to sudden damage under high stress, resulting in property losses (Meng et al. 2018). Therefore, there is an urgent need to elucidate the mechanism by which the microstructure of tight sandstone influences the propagation of cracks to prevent various types of engineering geohazards.

In this paper, based on XRD, BSE image scanning and EDS, targeted nanoindentation tests were conducted on the tight sandstone in Member 2 of the Xujiahe Formation in the Hechuan area, Sichuan Basin. (1) The micromechanical parameters and indentation patterns of different minerals under the same peak load were investigated, and the macroscopic rock mechanical parameters and fracture patterns of tight sandstone under stratigraphic temperature and pressure were examined via triaxial tests. (2) A mesoscopic compression finite element simulation was conducted using the Voronoi polygon-based global cohesive model, and the Young's modulus was compared after scaling via the homogenization method with the results of triaxial compression tests. (3) The macroscopic fracture mechanical behavior of tight sandstone was clarified from the micromechanical properties and damage mechanisms of minerals. (4) The relationships between the micromechanical properties of the tight sandstone constituent minerals and the macroscopic fracture modes and brittleness were determined.

2 Geological setting

The experimental samples were collected from the lower coal seam roof of Xujiahe Formation in the Hechuan area, in the southeastern part of the central paleo-uplift of the Sichuan Basin (Figs. 1a and b). The lithology of the Xu-I section is dominated by mudstone and coal beds, which are important hydrocarbon source rocks in the terrestrial stratal infill of the basin. The Xu-II section is the roof of the coal seams in the Xu- I section, and it shows a positive rhythm consisting of fine- to medium-grained feldspathic quartz sandstone, siltstone, and mudstone (Figs. 1c and d). The burial depth of the samples varies from 2100 to 2450 m.

3 Materials and methods

3.1 Sample preparation and experimental procedure

The experimental samples were obtained from tight sandstones in second member of Xujiahe Formation in the Hechuan area. A cylindrical sample with a diameter of 2.5 cm was laterally collared from the whole-diameter core using a diamond coring bit. Subsequently, the two end surfaces of the sample were carefully removed and smoothed until the sample achieved an aspect ratio of ≥ 2 and the required flatness for the test. After the completion of porosity and permeability experiments, as well as triaxial compression tests, the crushed column samples were fractured and cut for sampling, and small crushed samples were then taken for drying, grinding, and sieving through a 200 mesh. Powder compaction

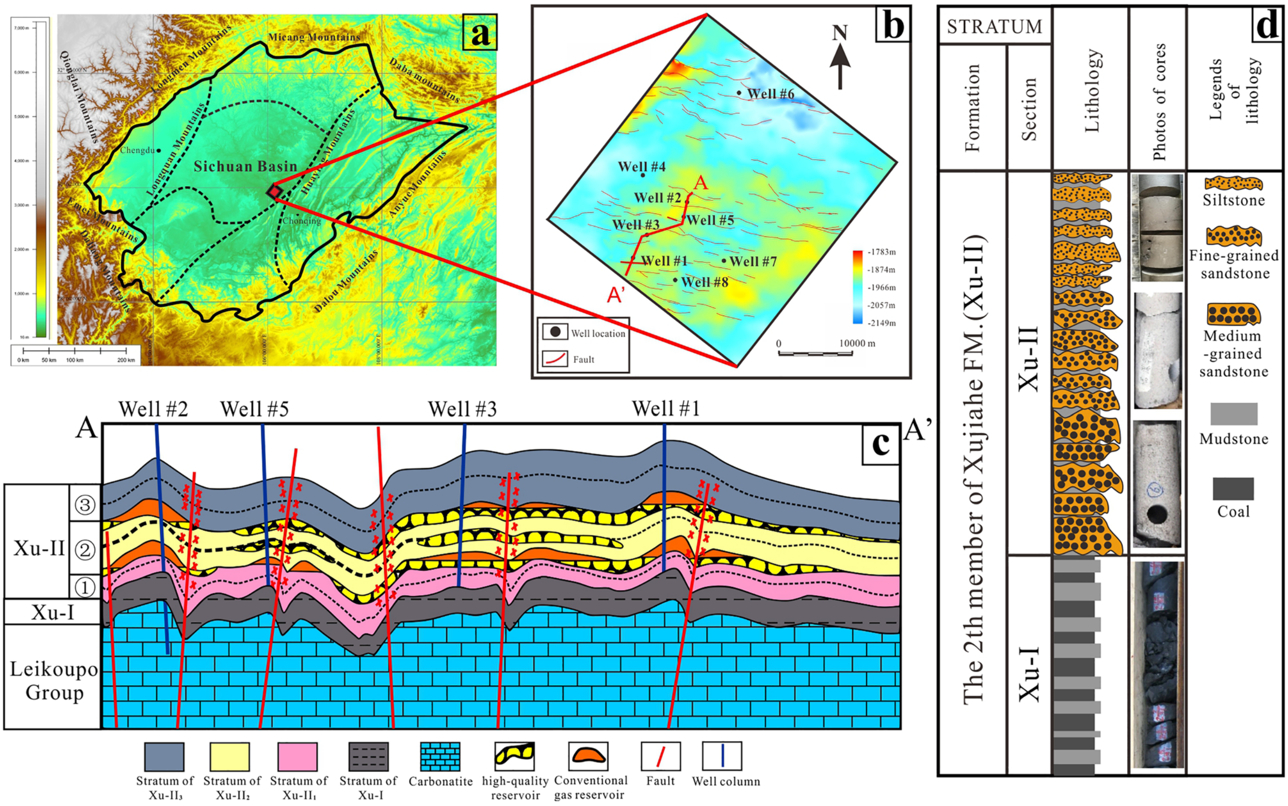

Fig. 1 **a** Tectonic units of the Sichuan Basin and location of the Hechuan area; **b** Tectonic setting of the Hechuan area and Sichuan Basin; **c** Schematic SW-NE cross section across the Hechuan area, Sichuan Basin; **d** Stratigraphic column through the Hechuan area, Sichuan Basin

was subsequently conducted, and the sample powder was positioned facing upward on a sample stage for XRD mineral analysis. Small intact internal cube samples were also taken from the crushed column samples for EDS and nanoindentation tests. The samples were initially shaped into cubic blocks measuring 15 mm × 8 mm × 3 mm mm through machining. Subsequently, the samples were cold-mounted with a low-viscosity epoxy resin. To ensure the accuracy of the nanoindentation testing data, it is necessary to address the issue of high surface roughness in the test samples (Donnelly et al. 2006). To achieve this, a sequential sanding process was employed using sandpapers with grit sizes of 800, 1200, 1500, 2000, 2500, and 3000. Additionally, the samples were further polished using an oil-based diamond polishing solution with particle sizes of 3 μm, 1 μm, and 0.5 μm. Then, the samples were cleaned in an ultrasonic instrument to remove any impurities. Finally, the samples were vacuum-dried to ensure that their roughness met the required standards for testing (Fig. 2).

3.2 Experimental methods

3.2.1 X-ray diffraction and particle size analysis

The mineralogical composition of the rocks was analyzed using an Ultima IV diffractometer from Rigaku Japan. The analysis was conducted at an ambient temperature of 25°C and a humidity of 30%. The parameters for whole-rock detection were set as follows: a starting angle of 5° and a termination angle of 50° for XRD. The scanning speed was set to 15°/m. For crystalline materials, if there is an angle between the crystal being examined and the incident X-ray beam, certain crystal planes that exhibit Bragg diffraction will be observed. This results in the appearance of diffraction peaks in the XRD pattern with varying intensities. The spectra were subsequently compared with the spectra in the standard library to identify the mineral species. Additionally, the intensity of the diffraction pattern was used to determine the relative proportion of each mineral. The particle size analysis was conducted through a series of steps, including image denoising, binarization, boundary extraction, multiscale segmentation of the rock thin section, and morphological analysis of the individual mineral particles using ImageJ software.

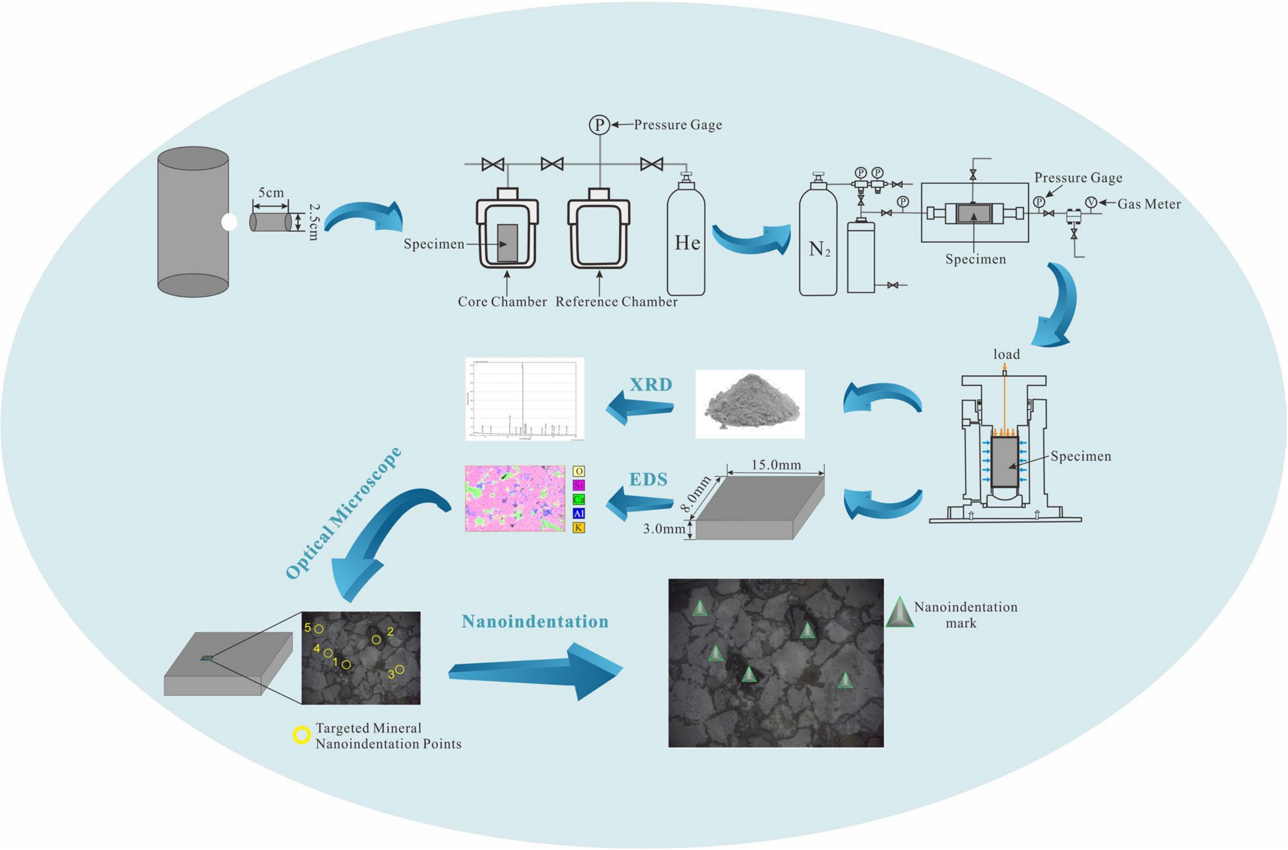

Fig. 2 Procedure for multiscale mechanical parameter testing of tight sandstone

3.2.2 Triaxial compression testing

Triaxial compression testing was conducted using the RTR-1500 triaxial rock mechanics servo testing system manufactured by GCTS, U.S.A. The maximum axial loading capacity of the testing system was 1500 kN, with an accuracy of 0.15% FS; the maximum confining pressure loading capacity and pore pressures were 140 MPa, with an accuracy of 0.1% FS; and the maximum temperature was 200°C, with an accuracy of 0.5°C (Figs. 3a and b). The experimental procedures and data processing methodologies utilized in this study are in strict compliance with the guidelines outlined by the International Society for Rock Mechanics (ISRM) for conducting rock triaxial testing. Additionally, these practices align with the established standards of the American Society for Testing and Materials (ASTM). The formation in situ pressure of the second member of the Xujiahe Formation ranges from 22.16 to 31.95 MPa, with pressure factors ranging from 1.01 to 1.49. Additionally, the distribution of formation temperatures ranges from 69.48 °C to 76.4°C, with a temperature gradient of 2.38°C/100 m. Therefore, triaxial compression testing was conducted at 70°C and a confining pressure of 30 MPa. The samples were initially placed in a sample compartment, in which the temperature and confining pressure were precisely controlled using the oil bath method, and axial stress was applied to the column samples (Fig. 3c). Transducers were utilized to record the axial and transverse strains, as well as the axial loads, exerted on the rock samples until the point at which the rock samples developed damage. The correlation between the compressive strength of the rock and the confining pressure was subsequently utilized to construct the molar stress circle to determine the shear strength characteristics (cohesion and angle of internal friction) of the rock under triaxial stress conditions. The Young's modulus (E) and Poisson's ratio (μ) of the sample are calculated from the linear elastic portion of the stress–strain curve by applying the following equations:

$$E = \frac{\Delta P \times H}{A \times \Delta H} \tag{1}$$

$$\mu = \frac{H \times d_{\mathrm{L}}}{\pi \times D \times H_{\mathrm{a}}} \tag{2}$$

where ΔP is the load increment, N; ΔH is the axial deformation increment, mm; H is the height of the sample, mm; A is the area of the sample, mm^2; d_{L} is the radial deformation, mm; and H_{a} is the axial deformation, mm.

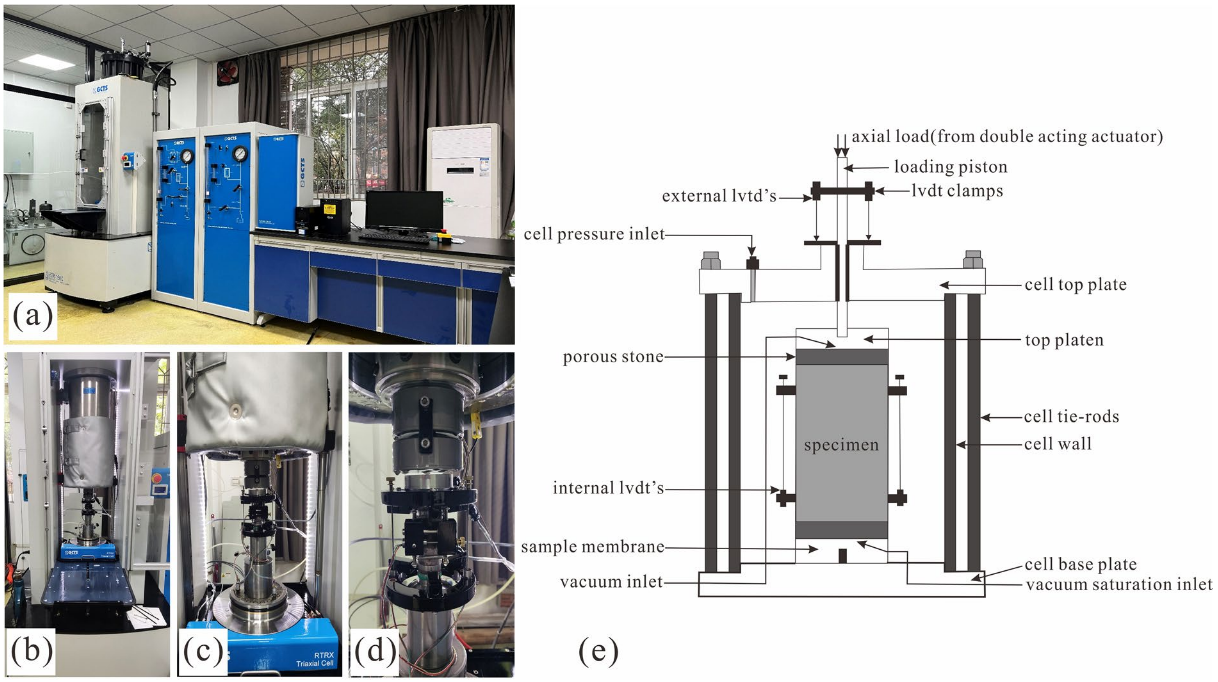

Fig. 3 **a** RTR-1500 rock mechanics test system; **b**, **c**, and **d** Detailed images of the axial loading system; **e** schematic of the axial loading system

3.2.3 Nanoindentation testing

Nanoindentation tests record the measurement of indenter displacement and the resulting load magnitude throughout the experiment, starting from the moment the indenter is pressed into the surface of the target mineral until the completion of the experiment. The three stages observed in the load–displacement curves correspond to pressure loading, continued loading, and pressure unloading stages of the nanoindentation testing process. The experiments were conducted using an Anton Paar NHT3 nanoindenter manufactured by CSM, Switzerland. The instrument can apply loads within a range of 0.1 to 500 mN, with a load precision of 0.02 mN. The indenter utilized in this study is of the diamond Berkovich type. This nanoindentation test adheres rigorously to the international standard for nanoindentation, ISO 14577 (International Organization for Standardization, 2015), and also followed the American Society for Testing and Materials standard, ASTM E2546 (American Society for Testing and Materials, 2015). The ambient temperature during the experiment was maintained at a consistent level of 23 ± 5°C, with a relative humidity of 45% ± 10%. Furthermore, the inclination of the specimen's test surface did not exceed 1°. To address potential concerns such as inadequate sample surface smoothness, size effects, and base effects that could influence indentation results, it is generally advised that the maximum indentation depth should be more than three times the surface roughness of the sample and less than one-tenth of the sandstone mineral grain size (Bobko and Ulm 2008; Abou-Chakra et al. 2010; Donnelly et al. 2006). Tight sandstone is characterized as a nonhomogeneous material with significant differences in the mechanical properties of its constituent minerals. These differences have a profound impact on the polishing outcome of the sample surface, resulting in a high roughness exceeding 100 nm. Therefore, $h_{\max}$ should be set at a value greater than 300 nm. The experimental samples reveal that 1/10 the size of the smallest siltstone grain is approximately 3900 nm, representing the value that $h_{\max}$ should not exceed. The maximum displacements of the four minerals (quartz, feldspar, calcite, and clay minerals) all ranged from 300 to 3900 nm only under an applied maximum load of 150 mN. During the loading process, the indenter was applied vertically to the mineral surface at a loading rate of 150 mN/min. As the applied load gradually increases, the indenter contacts the mineral surface. Initially, the mineral undergoes elastic deformation, followed by a transition to plastic strain. Subsequently, the load is held constant for a duration of 5 s. After this period, the indenter is unloaded from the mineral surface at a rate of 150 mN/min. During unloading, the mineral recovers from the deformation along the elastic path until the load reaches zero. At this point, the final indentation morphology is observable on the mineral surface (Fig. 4a).

Basic mechanical properties, such as Young's modulus and hardness of each mineral, can be calculated utilizing the characteristic parameters of the *P*–*h* curve (Hu and Li 2015). Figure 4b shows the typical load–displacement curves of minerals from nanoindentation tests, where $P_{\max}$

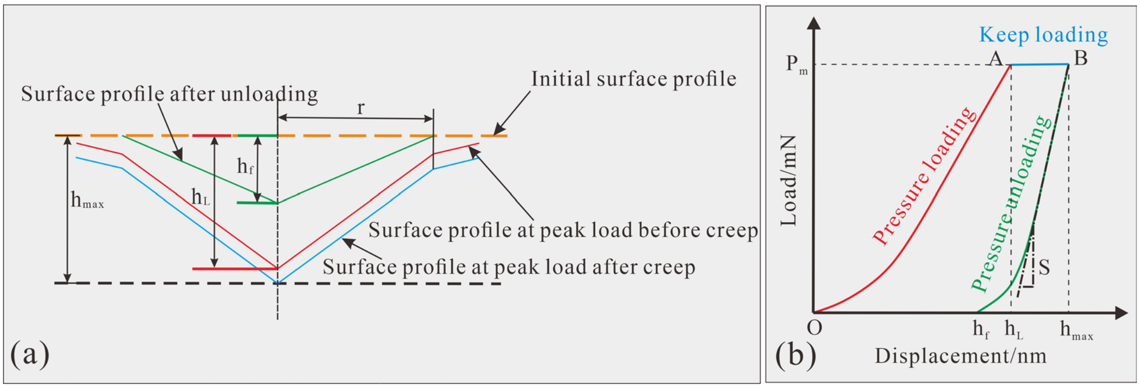

Fig. 4 Nanoindentation test diagrams. **a** Schematic of nanoindentation creep and elastic after effects (modified from reference (Sun et al. 2020a); **b** Schematic of the nanoindentation load–displacement curve (modified from reference (Hu and Li 2015)

is the maximum load, N; $h_{\max}$ is the maximum displacement, nm; h_{f} is the indentation depth after complete unloading, nm; and S is the elastic contact stiffness, N/m. Typically, the upper 25% to 30% of the unloading curve is fitted using least squares to derive Eq. (3), where α and m are the parameters obtained from least-squares fitting. Subsequently, the contact stiffness S is determined by employing Eq. (4):

$$P = \alpha\left(h - h_f\right)^m \tag{3}$$

$$S = \left(\frac{\mathrm{d}P}{\mathrm{d}h}\right)_{h=h_{\max}} \tag{4}$$

The Young's modulus E, hardness H and fracture toughness K_{c} are calculated by Eqs. (5)–(12) (Oliver and Pharr, 1992; Hu and Li 2015; Sun et al. 2020b):

$$h_{\mathrm{c}} = h_{\max} - \varepsilon \frac{P_{\max}}{S} \tag{5}$$

$$A_{\mathrm{c}} = \frac{3\sqrt{3}\tan\theta}{\cos\theta} h_{\mathrm{c}}^2 \tag{6}$$

$$E_{\mathrm{r}} = \frac{\sqrt{\pi}}{2\beta} \frac{S}{\sqrt{A_{\mathrm{c}}}} \tag{7}$$

$$\frac{1}{E_{\mathrm{r}}} = \frac{1 - v^2}{E} + \frac{1 - v_{\mathrm{i}}^2}{E_{\mathrm{i}}} \tag{8}$$

$$H = \frac{P_{\max}}{A_{\mathrm{c}}} \tag{9}$$

$$G_{\mathrm{C}} = \frac{W_{\mathrm{C}}}{A_{\max}} \tag{10}$$

$$A_{\max} = 24.5 h_{\max}^2 \tag{11}$$

$$K_{\mathrm{C}} = \sqrt{G_{\mathrm{c}} E_{\mathrm{r}}} \tag{12}$$

where h_{c} is the contact depth, nm; Ac is the projected area of the contact area, nm^2; $A_{\max}$ is the maximum cracked area, nm^2; W_{c} is the fracture energy, nJ; G_{c} is the critical energy release rate; ε is the constant related to the shape of the indenter; β is the correction factor of the indenter; θ is the angle between the center axis and the side of the indenter; and the Berkovich indenter is used in this experiment. Specifically, ε is 0.75, β is 1.034 and θ is 65.35°; E_{r} is the reduced modulus; $E_{\mathrm{i}} = 1141$ GPa is the indenter Young's modulus; $v_{\mathrm{i}} = 0.07$ is the indenter Poisson's ratio; and v is the Poisson's ratio of the minerals. From Eq. (6), it is evident that variations in the values of v have minimal impact on the calculated E, and a value of $v = 0.3$ is deemed appropriate. Additionally, E is the Young's modulus of minerals, GPa, and H is the hardness of minerals, GPa, K_{c} is the fracture toughness of minerals.

4 Results

4.1 Characterization of petrology

An analysis of 100 groups of thin section identification and particle size analyses reveals that feldspathic lithic sandstone is the dominant lithology within the study area (Fig. 5a). Based on this, the grain size has been employed to categorize the samples into three specific types: siltstone, fine-grained sandstone, and medium-grained sandstone. The grain size distributions of the different types of tight sandstone in the study area follow a normal distribution. The siltstone grain size distribution range is the most

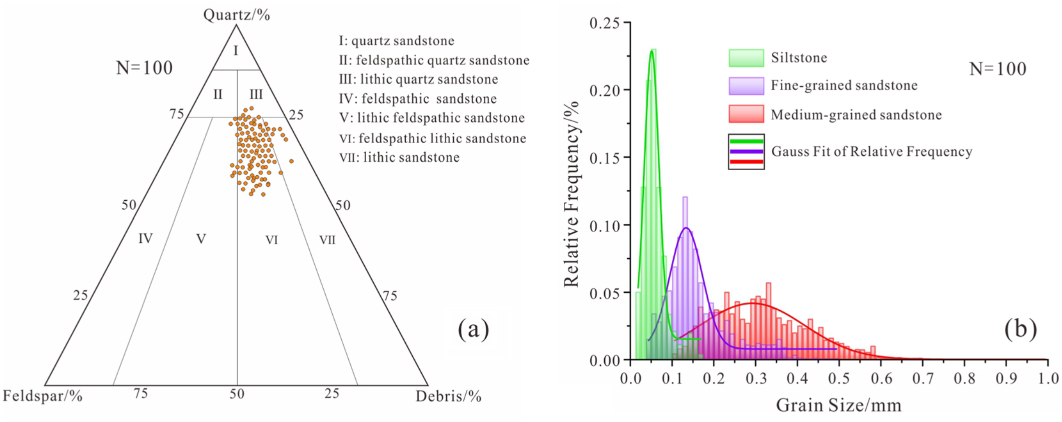

Fig. 5 **a** Lithology classification ternary plot; **b** Statistical distributions of grain size in the three types of tight sandstone

narrow, ranging from 0.0125 to 0.1750 mm, with a mean value of 0.0567 mm, and the mineral grains exhibit a high degree of roundness. The distribution of grain sizes in the fine-grained sandstone ranges from 0.0375 mm to 0.5 mm, with a mean value of 0.1601 mm. The medium-grained sandstone exhibits a broad range of grain size distributions, ranging from 0.1125 to 1 mm, with a mean value of 0.3159 mm; this feature represents the highest level of heterogeneity (Fig. 5b). The siltstone exhibits a lack of discernible pores and microfractures under a microscope; it has high compaction and cementation degrees. This means that this type of sandstone is relatively tight. The fine-grained sandstone samples exhibit a few primary pores and intergranular dissolution pores. The quantity of pores in the medium-grained sandstone is significantly greater than that in the siltstone and fine-grained sandstone. A few of these pores are primary pores with regular shapes and straight edges left behind during the process of sedimentation and burial, and most of them are irregularly distributed mixed pores consisting of primary pores and secondary pores, such as intergranular pores and intragranular pores (Fig. 6). The results indicated that the mean value of the porosity of the siltstone was 4.66%, and the mean value of the permeability was 0.14 mD. The mean value of the porosity of the fine-grained sandstone was 6.89%, and the mean value of the permeability was 0.21 mD. The

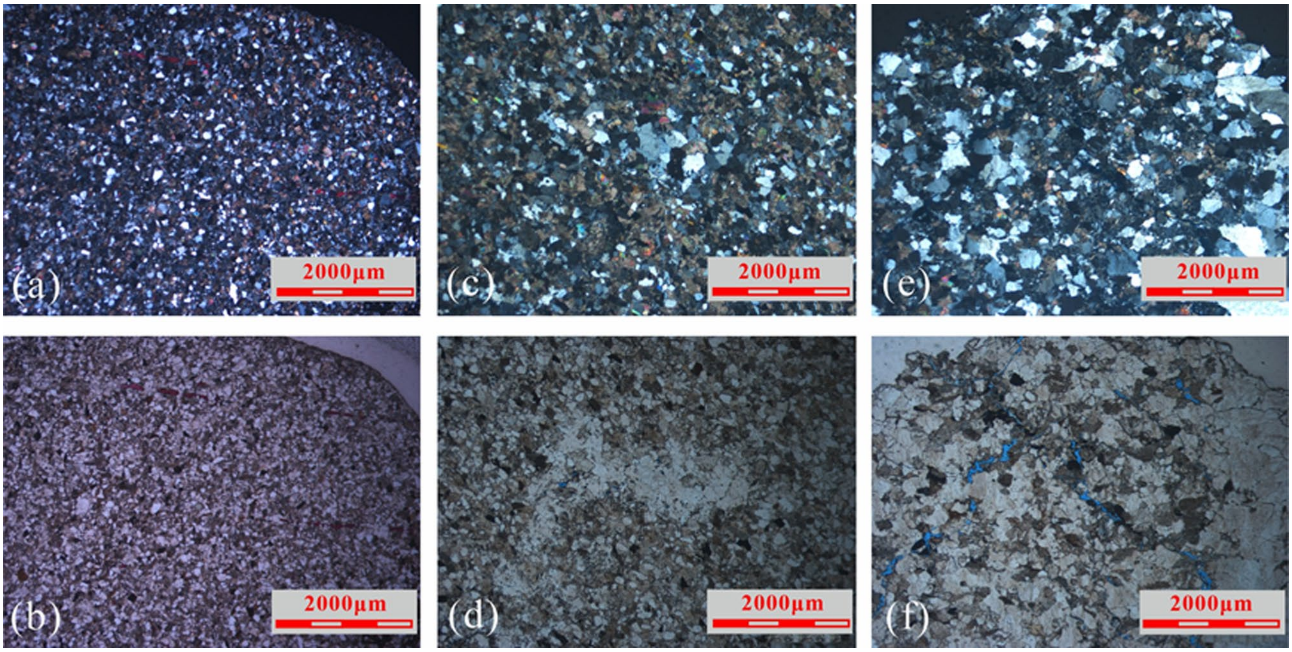

Fig. 6 Images of thin sections of different types of tight sandstone

mean value of the porosity of the medium-grained sandstone was 8.71%, and the mean value of the permeability was 0.54 mD. The petrophysical properties of the rocks exhibit clear regularity, with porosity and permeability of siltstone < fine-grained sandstone < medium-grained sandstone. This trend aligns with the thin section identification shown in Table 1.

The XRD results indicate that quartz is the predominant mineral in all types of tight sandstones, comprising an average percentage exceeding 60%. Specifically, the average percentage of quartz in the siltstone is 61.83%, and the percentages in the fine-grained and medium-grained sandstones are 65.23% and 68.15%, respectively. Feldspar is a secondary constituent, with an average percentage of approximately 20% (including both potassium feldspar and plagioclase feldspar) in the three types of tight sandstones. The clay minerals, which predominantly are the cement, differ slightly among the three types of sandstones, with percentages of 16.23% in the siltstone, 13.50% in the fine-grained sandstone, and 10.89% in the medium-grained sandstone. Calcite is another cement type, accounting for a very small proportion of the total, wherein the differences in proportions among the different types of sandstones are not readily discernible. In summary, the study revealed a consistent trend in the mineral composition of the tight sandstone samples. Specifically, as the grain size decreases, the quartz content of the tight sandstone decreases, while the clay mineral content increases (Table 1). The samples were analyzed using a high-resolution scanning mode that involved a combination of BSE image scanning and EDS analysis. The findings reveal that the sample primarily consisted of the element silicon (Si), followed by potassium. (K) and calcium (Ca), with some aluminum also present. Combined with the XRD results, Si is found to exhibit a predominantly granular distribution, specifically in the form of quartz mineral aggregates. Additionally, some Si is observed at the interfaces between mineral grains. This result suggests the presence of silicate-like cement. Most of the K exhibits a patchy distribution (i.e., confined to potassium feldspar minerals) and the remaining K is scattered throughout samples. Potassium may form impurities in quartz grains. Calcium is present as elongated bars or masses and mainly constitutes calcite. Aluminum (Al) is commonly present in clay minerals and feldspar. In addition, the high-resolution scanning results reveal that the mineral grains exhibit strong cementation and are devoid of discernible microfractures or significant pores (Fig. 7).

4.2 Results of nanoindentation tests

4.2.1 *P–h* curve characteristics and microscopic fracture behavior

The load─displacement curve records the nonlinear mechanical responses between the indenter and mineral during the indentation process (Ohmura and Wakeda 2021). Nanoindentation tests were performed on the same composition and different crystalline forms of minerals in the same macroscale sample, and differences in micromechanical properties and mechanical responses were found. As shown in Fig. 8, curves a and b represent the *P–h* curves of monocrystalline quartz (measurement point 2) and polycrystalline quartz (siliceous debris; measurement point 1), respectively. The *P–h* curve a is typically smooth, while curve b exhibits an obvious pop-in phenomenon during the loading stage. Since siliceous debris has a lower initial fracture stress than monocrystalline quartz, the first pop-in point in curve b indicates that the load has reached the yield strength of the siliceous debris. In addition, initial brittle fracturing occurs. The indenter instantly loses the support of the mineral surface and advances rapidly. As the load continues to increase, the initial microcracks gradually propagate and come into contact with the internal defects of the mineral itself, and the second and third pop-in event points occur. By comparing the residual morphologies of the two groups of indentation tests (Fig. 8), it was found that the residual indentation of monocrystalline quartz at measurement point 2 of sample N9 was clear and highly consistent with the shape of the indenter. Furthermore, no additional cracks can be observed. The residual indentation of the siliceous debris at measurement point 1 of sample N9 had obvious radial cracks and bending near the end. The bending phenomenon indicated the occurrence of fracture instability, and the indentation phenomenon corresponded to the nonlinear mechanical response events recorded in curve b. Furthermore, by comparing curves a and b, it was found that curve b exhibits an elbow-shaped phenomenon in which the slope of the curve suddenly decreases during the unloading stage. The reason for this phenomenon is that under the high pressure of the indenter, the internal structure of the siliceous mineral is subjected to a high pressure, resulting in material phase transformation and swelling. These findings show that even though both quartz and siliceous debris are siliceous minerals, the micromechanical properties are significantly different due to differences in microscopic mineral grain size and structure; moreover, the structure and mechanical properties of monocrystalline quartz are more stable than those of siliceous debris. Compared with quartz, siliceous debris with a fine-grained polycrystalline structure is weaker, and its crystal structure is more easily damaged, resulting in brittle fracture and phase transformation.

Table 1 Analysis results of mineral composition and petrophysical property in tight sandstone

Sample	Well number	Depth (m)	Tight sandstone Types	Mineral composition (wt%)					Porosity (%)	Permeability (mD)
				Clay mineral	Quartz	potash feldspar	plagioclase feldspar	Calcite		
N1	Well #1	2424.05	Medium-grained sandstone	7.5	72.2	8.6	10.4	1.3	8.0	0.183
N2	Well #1	2431.95	Medium-grained sandstone	9.4	69.3	12.5	7.2	1.6	12.8	2.340
N3	Well #1	2404.80	Fine-grained sandstone	12.1	59.3	4.5	22.8	1.3	7.0	0.214
N4	Well #1	2414.20	Fine-grained sandstone	12.8	63.2	8.1	14.8	1.1	8.9	0.235
N5	Well #2	2215.60	Siltstone	10.7	63.8	13.0	11.2	1.3	6.6	0.191
N6	Well #3	2115.30	Fine-grained sandstone	8.2	70.8	7.9	11.9	1.2	6.3	0.120
N7	Well #4	2241.30	Medium-grained sandstone	10.1	65.2	8.9	13.9	1.9	6.6	0.203
N8	Well #5	2187.10	Medium-grained sandstone	17.4	68.2	6.8	6.4	1.2	8.4	0.461
N9	Well #6	2289.90	Siltstone	16.3	56.2	10.8	15.6	1.1	5.8	0.190
N10	Well #6	2274.50	Siltstone	18.1	60.6	8.3	11.2	1.8	5.6	0.284
N11	Well #6	2297.10	Fine-grained sandstone	13.5	60.1	6.1	20.3	0.0	7.3	0.188
N12	Well #3	2143.70	Fine-grained sandstone	14.8	69.6	6.8	8.8	0.0	6.0	0.247
N13	Well #5	2181.90	Siltstone	17.8	65.5	9.7	3.4	3.6	6.2	0.121
N14	Well #7	2231.20	Siltstone	19.6	60.2	6.7	13.5	0.0	6.1	0.225
N15	Well #7	2263.30	Siltstone	16.4	61.8	13.6	8.2	0.0	2.7	0.041
N16	Well #4	2230.00	Siltstone	15.7	62.3	8.8	13.2	0.0	2.2	0.052
N17	Well #1	2419.05	Fine-grained sandstone	13.6	64.5	7.8	12.2	1.9	6.2	0.180
N18	Well #1	2438.15	Medium-grained sandstone	9.9	63.8	8.7	15.5	2.1	7.0	0.293
N19	Well #8	2113.45	Siltstone	15.2	64.2	7.8	12.8	0.0	2.1	0.038
N20	Well #8	2129.25	Fine-grained sandstone	10.4	70.6	6.8	9.8	2.4	6.4	0.198
N21	Well #8	2146.35	Fine-grained sandstone	19.9	67.1	4.3	8.7	0.0	7.0	0.334
N22	Well #8	2149.90	Medium-grained sandstone	11.5	62.5	10.5	15.5	0.0	10.4	0.293
N23	Well #8	2151.85	Medium-grained sandstone	9.2	70.1	7.2	12.3	1.2	8.7	0.313
N24	Well #8	2157.05	Medium-grained sandstone	9.5	76.8	6.3	7.4	0.0	7.8	0.235

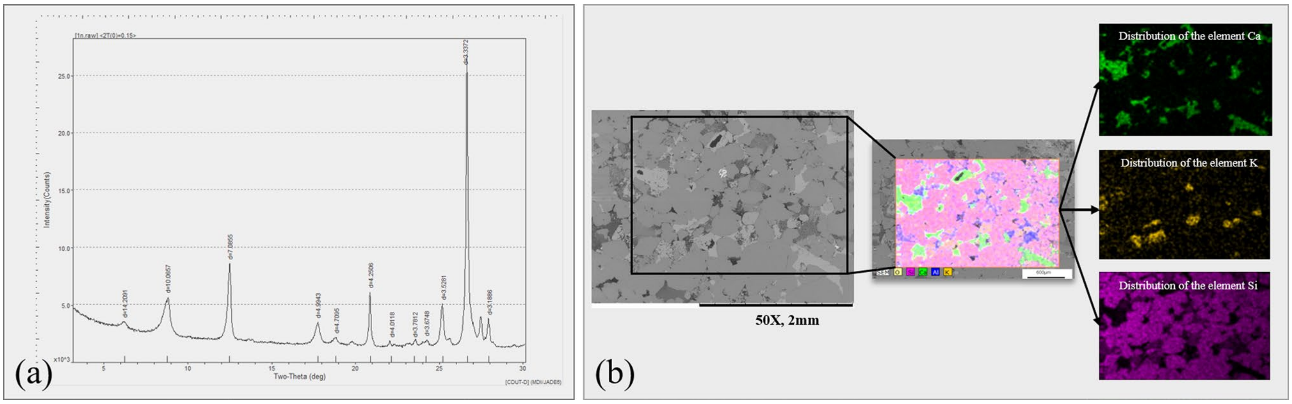

Fig. 7 **a** Sample N1 Well #1, 2404.8 m, XRD pattern; **b** Sample N1, Well #1, 2404.8 m. The mineral distribution was obtained via EDS analysis

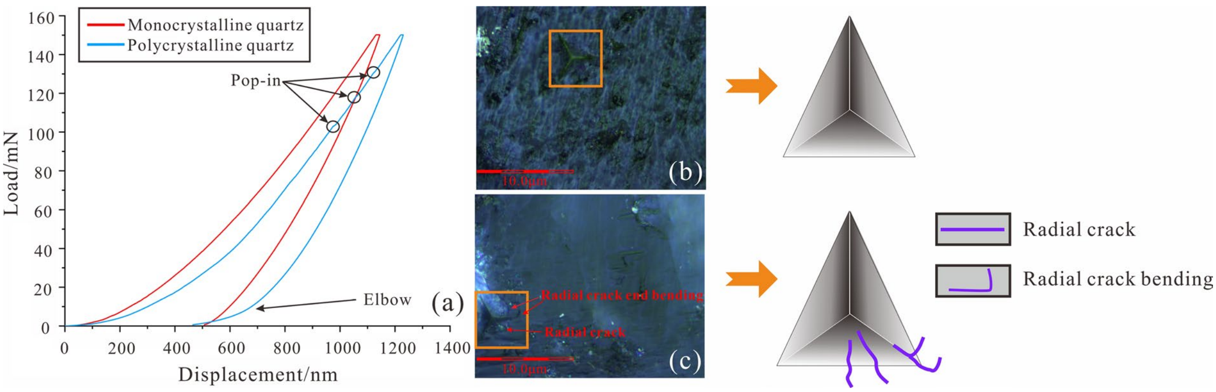

Fig. 8 Typical indentation curves and indentation topography images of monocrystalline and polycrystalline quartz. **a** Indentation curves; **b** Topography image of monocrystalline quartz (N9-2 test point, quartz); **c** Topography image of polycrystalline quartz (N9-1 test point, siliceous debris)

Different mineral crystal structures also lead to different mechanical responses. By comparing the *P*–*h* curves of quartz, feldspar, calcite and clay minerals in the four groups of samples (N1 to N4; the samples were all from Member 2 of the Xujiahe Formation in Well #1) (Fig. 9a), it was found that under the same load conditions, quartz exhibits the smallest maximum displacement, the largest restoration of elastic deformation in the unloading stage, the *P*–*h* curve with the smallest dispersion, and smooth loading and unloading curves. The indentation showed a regular morphology that matched the shape of the indenter and was small in size, and no obvious brittle or plastic cracks could be observed in the surrounding area (Fig. 9b). The *P*–*h* curves and indentation morphologies both show that quartz has a tight structure and strong micromechanical properties. Under the same loading conditions, the overall maximum displacement of feldspar is slightly greater than that of quartz, the degree of dispersion of its *P*–*h* curve is greater than that of quartz, and the topographic images of individual residual indentations reveal radial cracks representing brittle fractures (Fig. 9c). However, the maximum displacement of calcite is greater than that of the above two minerals, and the pop-in phenomenon generally appears in the loading stage of the *P*–*h* curve with a high degree of dispersion. These characteristics indicate that the calcite structure is relatively loose and that the micromechanical properties are relatively weak. Compared with those of the above two minerals, the morphological regularity of the residual indentations of calcite is significantly lower, the indentation exhibits unwanted deformation (plastic distortion) due to the shape of the indenter, and a small number of microscopic shear cracks representing plasticity appear near the triangular indentation (Fig. 9d). The maximum displacement, the displacement variable at the maintaining load stage, and the morphologies of the residual indentations of the clay minerals are all much greater than those of the quartz, feldspar, and calcite. Furthermore, there are many shear bands and large amounts of plastic chipping damage in the triangular dents (Fig. 9e). The recovery deformation during the unloading stage is small. This indicates that the clay minerals are the softest.

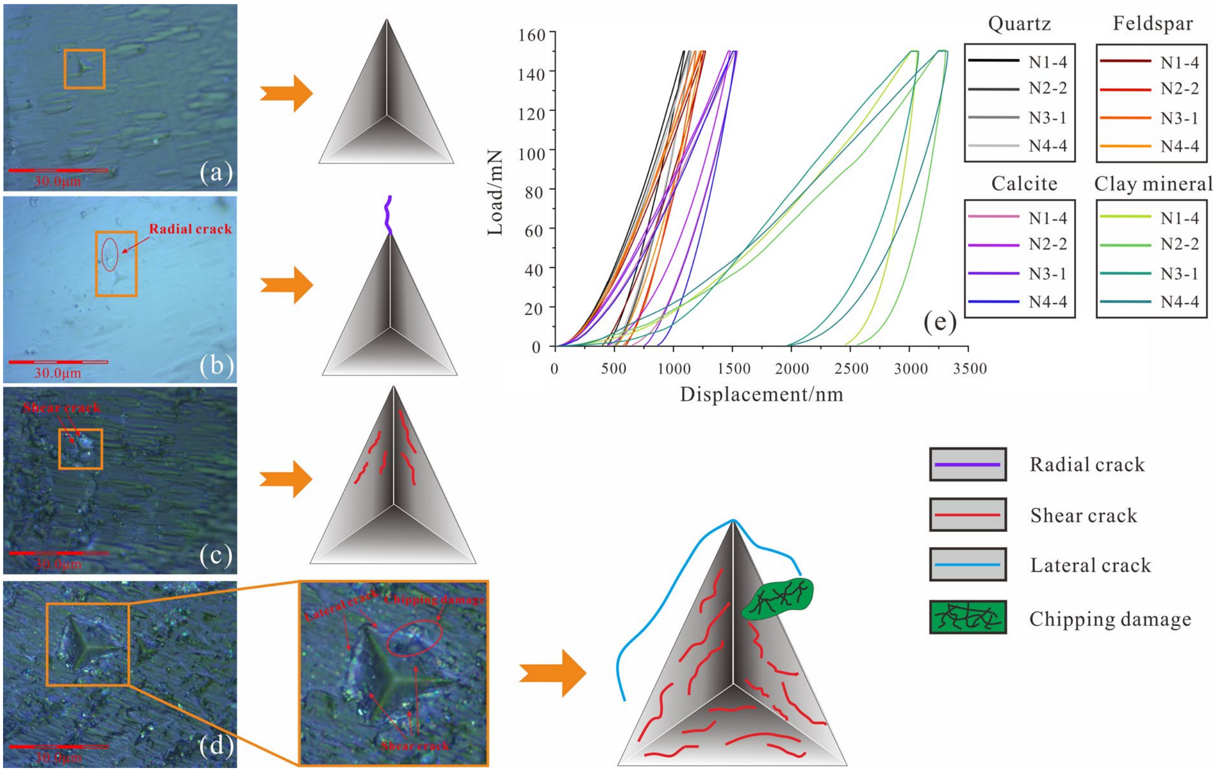

Fig. 9 Typical indentation curves and corresponding indentation topography images of compositional minerals. **a** Topography image of quartz (N4-5 test point); **b** Topography image of feldspar (N4-4 test point); **c** Topography image of calcite (N4-1 test point); **d** Topography image of clay minerals (N4-3 test point); **e** Indentation curves

Because the clay minerals are mostly matrix minerals tat fill gaps between large skeleton mineral grains, the *P*–*h* curve generally exhibits an elbow phenomenon in the unloading stage. Additionally, the clay minerals mostly have layered or layer–chain structures. The special molecular structure of the mineral makes the interlayer structure prone to structural defects, such as dislocations and gaps. In addition, there are various types and complex structures that have different structural and combination characteristics at the nanoscale; thus, the material has strong nonhomogeneity, and the *P*–*h* curve has the largest degree of dispersion (Xing et al. 2017). In summary, as hard minerals, quartz and feldspar do not easily fail, and in some cases, they have radial cracks reflecting brittle failure behavior. In contrast, minerals with greater plasticity have weaker and more unstable mechanical properties, larger indentation morphologies, and more fragile fractures. Shear cracks caused by plastic deformation are likely to occur and can develop into transverse cracks and surface spalling.

The *P*–*h* curve can reflect the energy change during the nanoindentation process (Cheng et al. 2002; Gupta et al. 2020). As shown in Fig. 4b, the integrated area of OABh$_m$ represents the total work W_t, and the integrated area of h$_f$Bh$_m$ under the unloading curve represents the elastic work W_e. The elastic work ratio parameter ($W=W_e/W_t$) was established to characterize the different minerals quantitatively. A larger W indicates stronger elastic–plastic properties of the mineral. By utilizing energy, it is feasible to determine the fracture toughness, K_c, which suggests the capacity of mineral type to withstand crack destabilization. Similarly, energy and fracture toughness calculations were performed on the four types of minerals, namely, quartz, feldspar, calcite, and clay minerals, in the four groups of samples (N1 to N4). The samples were from Submember 2 of Member 2 of the Xujiahe Formation in Well #1. The results are shown in Table 2. The average *W* and K_c values of quartz are 0.62 and 2.29 MPa·m$^{0.5}$, the highest among the four minerals, indicating that quartz is a typical elastic mineral and the hardest to crack. The average W values for feldspar and calcite are 0.60 and 0.50, respectively, whereas the average K_c values are 1.90 MPa·m$^{0.5}$ and 1.41 MPa·m$^{0.5}$, respectively. Clay minerals exhibit the smallest values for *W* and K_c, with average values of 0.23 and 0.82 MPa·m$^{0.5}$, respectively. It is characterized by strong plastic properties and lower cracking difficulty than other mineral types. It can be observed from the preceding analysis that minerals with higher plasticity exhibit lower fracture toughness, making them more susceptible to cracking. However, these plastic minerals predominantly generate plastic cracks, which can rapidly lead to failure due to accelerated damage propagation

Table 2 Energy values of diagenetic minerals based on *P–h* curves

Mineral Species	Test point number	W_e (nJ)	W_t (nJ)	W_e/W_t	Average W	K_c (MPa·m$^{0.5}$)	Average K_c (MPa·m$^{0.5}$)
Quartz	N1-2	40.87	61.95	0.66	0.62	2.35	2.29
	N2-5	38.31	65.89	0.58		2.25	
	N3-2	38.72	63.37	0.61		2.33	
	N4-5	40.68	65.27	0.62		2.22	
Feldspar	N1-4	54.59	74.77	0.73	0.60	1.68	1.90
	N2-2	41.77	75.58	0.55		1.78	
	N3-1	35.00	66.93	0.52		2.30	
	N4-4	44.48	73.70	0.60		1.82	
Calcite	N1-3	48.01	91.76	0.52	0.50	1.39	1.41
	N2-4	54.28	90.77	0.60		1.35	
	N3-5	45.42	96.47	0.47		1.31	
	N4-1	37.71	88.78	0.42		1.61	
Clay mineral	N1-1	27.43	165.01	0.17	0.23	1.07	0.82
	N2-1	32.39	181.58	0.18		0.86	
	N3-4	49.87	172.11	0.29		0.78	
	N4-3	59.14	203.07	0.29		0.57	

at a macroscopic level and an increased propensity for single fracture formation. In contrast, brittle minerals, characterized by their high fracture toughness, are inherently more resistant to cracking. They tend to generate stable brittle cracks, resulting in a slower progression of damage on a macroscopic scale and a tendency towards complex fracture patterns.

4.2.2 Young's modulus and hardness characteristics of minerals

For the tight sandstone roof of coal seam in the study area, 10 groups of targeted nanoindentation tests were carried out with a total of 50 peak loads with magnitudes of 150 mN each. The targeted minerals included the following four minerals: quartz, feldspar, calcite, and clay minerals. A small amount of quartz debris was present (Table 3). The test results showed that quartz has the highest Young's modulus and hardness, with mean values of 92.46 ± 9.42 GPa and 12.53 ± 2.42 GPa, respectively, followed by feldspar, with mean values of 71.85 ± 9.69 GPa and 6.50 ± 1.79 GPa, respectively; calcite, with mean values of 48.28 ± 7.34 GPa and 4.40 ± 1.16 GPa, respectively; and clay minerals, with the lowest modulus and hardness, with mean values of 27.63 ± 10.81 GPa and 0.79 ± 0.23 GPa, respectively. The results of Young's modulus and hardness obtained from the nanoindentation test are consistent with the elastic plasticity of different minerals, as reflected by the energy change calculated from the *P–h* curve above.

In addition, the degrees of dispersion of the micromechanical parameters obtained from the tests of the four types of minerals were analyzed. There are significant differences in the mechanical parameters of the different minerals. For example, the difference in the hardnesses of quartz and clay minerals spans an order of magnitude, and the standard deviation cannot accurately characterize the dispersion. Therefore, the coefficient of variance was introduced. According to the results, the coefficients of variance of the Young's modulus values of the four minerals (quartz, feldspar, calcite, and clay minerals) are 0.102, 0.135, 0.152, and 0.391, respectively, and the coefficients of variance of the hardnesses are 0.193, 0.258, 0.263, and 0.289, respectively. The micromechanical parameters of quartz have the lowest degree of dispersion, those of feldspar and calcite are intermediate, and those of clay minerals have the highest degree of dispersion (Fig. 10). Based on the *P–h* curve and indentation residual morphology characteristics, the crystal structures and mechanical properties of minerals with stronger mechanical properties are considered more stable and less likely to be damaged; additionally, minerals with strong plasticity have weak mechanical properties, an unstable and heterogeneous structure, and a high dispersion of micromechanical properties and are more susceptible to plastic failure.

4.3 Results of the macroscopic triaxial tests

4.3.1 Characteristics of stress–strain curves and macroscopic fracture behavior

The stress–strain curve documents the complete process of tight sandstone fracture under compression, which can be segmented into five stages: Stage I is the stress stabilization stage, during which the pores and microcracks in the rock start to close as compression initiates. Stress increment is gradual, strain increases rapidly, and the curve displays a slightly concave pattern. Stage II

Table 3 Results of the nanoindentation tests of the microscopic mechanical parameters

Sample	Test point number	Well number	Depth (m)	Maximum load (mN)	Hardness (GPa)	Young's modulus (GPa)	Mineral species
N1	1	Well #1	2404.8	150	1.13	25.13	Clay mineral
	2				13.86	101.41	Quartz
	3				3.07	32.02	Calcite
	4				4.21	77.57	Feldspar
	5				5.55	86.52	Quartz debris
N2	1	Well #1	2414.2	150	0.95	22.71	Clay mineral
	2				3.78	68.57	Feldspar
	3				11.75	94.84	Quartz
	4				4.89	36.94	Calcite
	5				11.61	84.42	Quartz
N3	1	Well #1	2424.05	150	7.63	87.87	Feldspar
	2				10.77	81.62	Quartz
	3				4.26	44.36	Calcite
	4				0.67	18.77	Clay mineral
	5				5.40	53.89	Calcite
N4	1	Well #1	2431.95	150	2.53	57.65	Calcite
	2				10.10	113.70	Quartz
	3				0.70	18.30	Clay mineral
	4				7.09	68.59	Feldspar
	5				14.35	99.65	Quartz
N5	1	Well #2	2215.6	150	4.41	51.01	Calcite
	2				10.59	79.24	Quartz
	3				0.80	24.31	Clay mineral
	4				9.60	56.76	Feldspar
	5				4.14	58.32	Calcite
N6	1	Well #3	2115.3	150	0.65	30.60	Clay mineral
	2				5.52	50.61	Calcite
	3				11.61	84.42	Quartz
	4				0.74	42.01	Clay mineral
	5				8.31	67.58	Feldspar
N7	1	Well #4	2241.3	150	6.31	60.88	Feldspar
	2				13.13	89.96	Quartz
	3				6.34	47.53	Calcite
	4				0.67	20.40	Clay mineral
	5				11.52	85.69	Quartz
N8	1	Well #5	2187.1	150	15.53	96.98	Quartz
	2				7.60	86.55	Feldspar
	3				2.45	48.45	Calcite
	4				0.42	7.30	Clay mineral
	5				1.29	38.91	Clay mineral
N9	1	Well #6	2289.9	150	7.24	79.93	Quartz debris
	2				10.12	85.35	Quartz
	3				4.57	48.33	Calcite
	4				0.91	41.94	Clay mineral
	5				7.97	67.25	Feldspar

Table 3 (continued)

Sample	Test point number	Well number	Depth (m)	Maximum load (mN)	Hardness (GPa)	Young's modulus (GPa)	Mineral species
N10	1	Well #6	2297.1	150	11.32	102.69	Quartz
	2				19.17	94.49	Quartz
	3				5.21	50.21	Calcite
	4				0.61	41.12	Clay mineral
	5				2.53	76.88	Feldspar

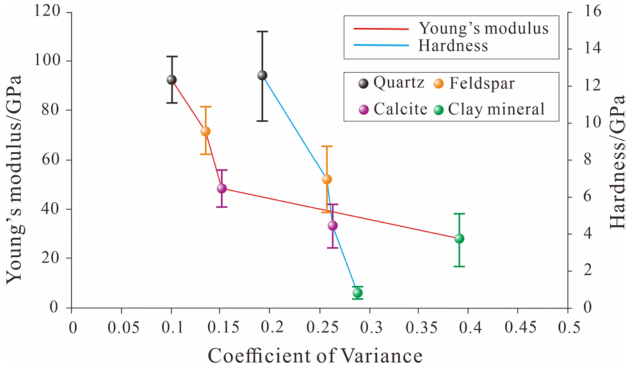

Fig. 10 Mean and coefficient of variance of microscopic mechanical parameters of compositional minerals

is the linear elasticity stage, characterized by a nearly straight curve, maintaining Young's modulus as a constant. Stage III represents the stable crack propagation stage, where predominantly stable cracks form, leading to a decrease in Young's modulus with strain increase, resulting in a nonlinear convex curve. Stage IV marks the unstable crack propagation stage, initiated when the load reaches the crack extension stress, signifying the onset of intolerable damage in tight sandstone. Stage V, the post-peak stage, involves unloading the load, leading to a sharp decline in the curve.

The stress–strain curves of the three types of tight sandstones were plotted, as illustrated in Fig. 11. The progressive compressive fracture process of different tight sandstones exhibits distinct characteristics. Based on the statistical analysis of the petrological features outlined in Sect. 3.1, the mineral particle size and the degree of non-uniformity follow an increasing order in siltstone, fine-grained sandstone, and medium-grained sandstone. During the linear elasticity phase (Stage II), an increase in mineral particle size and inhomogeneity leads to a shorter Stage II duration, a decrease in the slope of the curve (Young's modulus), and a slight increase in axial strain, indicating a loss of linear elasticity characteristics. In the stable crack propagation phase (Stage III), tight sandstone with larger mineral particle sizes and higher degrees of heterogeneity tends to experience crack initiation and damage at lower stresses. When two independently sprouted cracks become interconnected, the stable crack extension stage transitions to the unstable crack extension stage, marking the onset of the strain localization stage (Stage IV). The larger the mineral particle size and inhomogeneity of tight sandstones, the shorter the strain localization phase, leading to quicker attainment of peak stress and macroscopic damage following crack extension. In the post-peak stage (Stage V), characterized by larger mineral particle sizes and increased inhomogeneity in tight sandstone, the rate of strength loss decreases. Nevertheless, the residual strengths following peak stress for the three categories of tight sandstones remain relatively consistent.

In terms of the corresponding fracture modes, the fracture mode of siltstone is mostly single-shear failure, and that of fine-grained sandstone mostly exhibits double-shear failure. The medium-grained sandstone is dominated by multiple longitudinal splitting failures or more complicated Y-shaped splitting–shear composite failures (Fig. 11).

4.3.2 Study of the macroscopic rock mechanical parameters and characteristic stress points

The experimental results indicate that Young's modulus of the siltstone is 28.52 ± 5.67 GPa, accompanied by a Poisson's ratio of 0.163 ± 0.050. Similarly, the fine-grained sandstone exhibits a Young's modulus of 20.76 ± 1.25 GPa, with a Poisson's ratio of 0.199 ± 0.053. Additionally, the medium-grained sandstone has a Young's modulus of 19.76 ± 0.94 GPa, along with a Poisson's ratio of 0.223 ± 0.054 (Fig. 12a). The Young's modulus of siltstone exhibits a significantly greater degree of discreteness than that of fine-grained sandstone and medium-grained sandstone. Based on the results from the nanoindentation tests, it is evident that the clay minerals exhibit the lowest mechanical stability. Additionally, it is noteworthy that the clay mineral content in siltstone is much greater than that in the other two types of

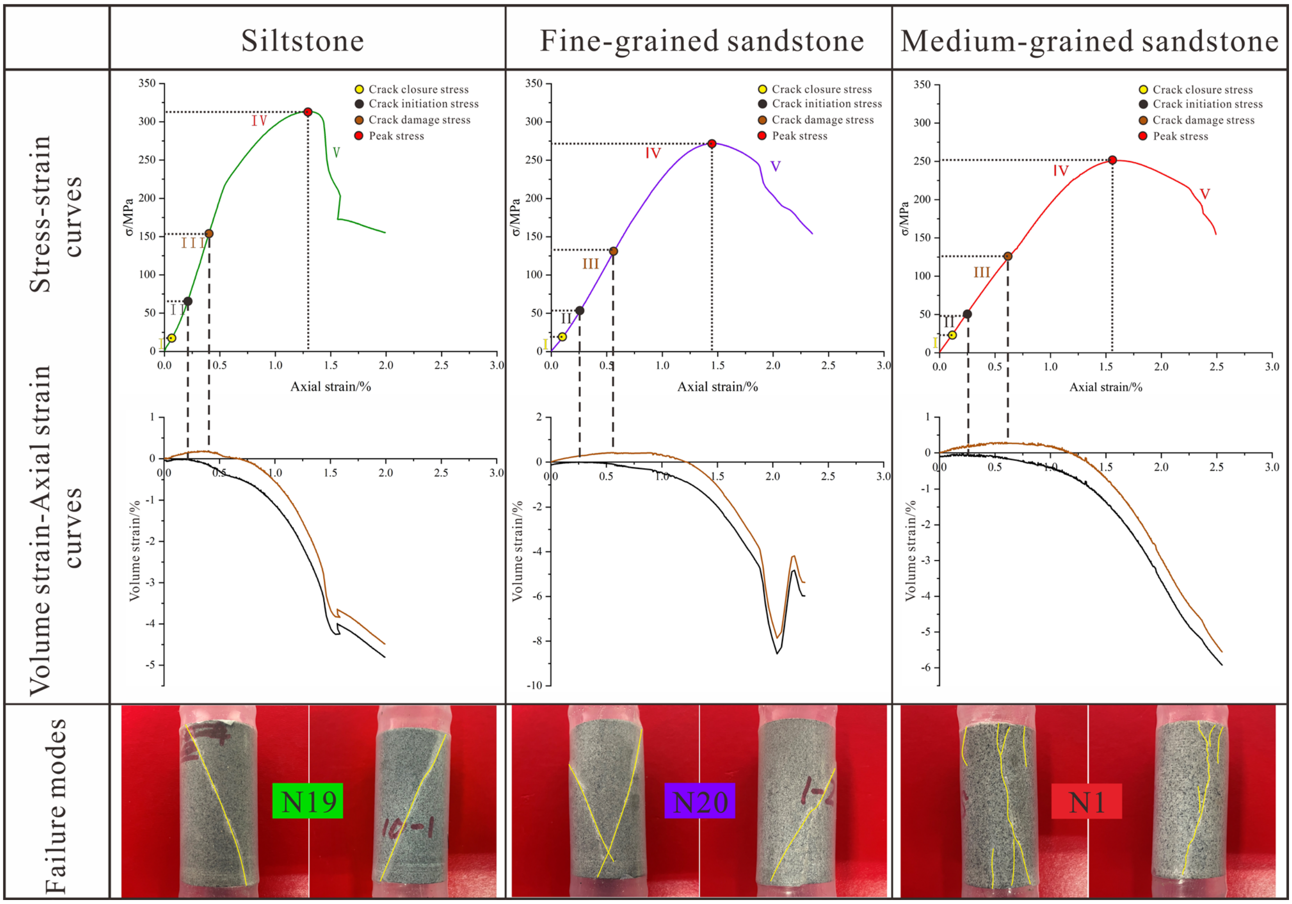

Fig. 11 Typical stress–strain curves and corresponding failure mode images of tight sandstone

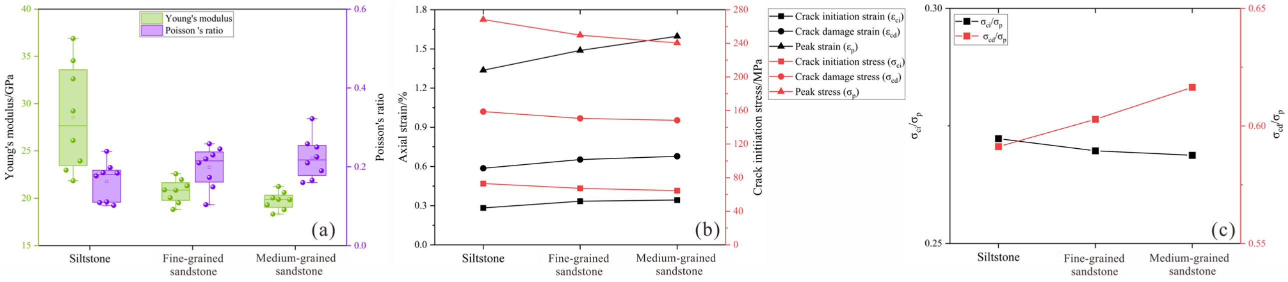

Fig. 12 **a** Statistical analysis of the macroscopic mechanical parameters of the tight sandstone specimens; **b** Statistical analysis of characteristic stresses and characteristic strains in tight sandstone specimens; **c** Statistical analysis of normalized stress thresholds and normalized strain thresholds in tight sandstone specimens

tight sandstone. Therefore, the presence of relatively high clay mineral content has an impact on the stability of the macromechanical properties of siltstone to a certain degree. Overall, the Young's modulus of tight sandstone decreases, and Poisson's ratio increases with increasing grain size.

To elucidate the distinctions in characteristic features among various types of tight sandstones, an analysis was conducted on the statistics of crack initiation stress points (σ_{ci}), crack damage stress points (σ_{cd}), and peak stress points for 24 sets of tight sandstones. The characteristic stress values σ_{ci} and σ_{cd} are derived from the cracked volumetric strain-axial strain curve. The crack initiation stress σ_{ci} is identified as the bias stress at the inflection point where the curve transitions from a gradual tendency to 0, while the bias stress at the peak of the volumetric strain (occurring when the sample is compressed to a minimum volume) denoted as σ_{cd}. The statistical findings indicate a consistent trend across all three characteristic stress values (σ_{ci}, σ_{cd}, and σ_p) with siltstone exhibiting the highest values, followed by fine-grained sandstone, and then medium-grained sandstone. Conversely, the strain values corresponding to these characteristic stresses demonstrate a contrasting trend, as illustrated in Fig. 12b. Additionally, normalized stress thresholds were calculated to better represent the characteristics of the variation in characteristic stress thresholds. It was observed that the normalized crack initiation stress (σ_{ci}/σ_p) decreases with increasing mineral particle size and degree of inhomogeneity, while the normalized crack damage stress (σ_{cd}/σ_p) increases with increasing mineral particle size and degree of inhomogeneity (Fig. 12b). This suggests that medium-grained sandstone exhibits a lower stress resistance, leading to the early formation of cracks. Once unstable cracks emerge macro-damage is more likely to occur rapidly, primarily attributed to stress concentration within the medium-grained sandstone specimens. The intricate development of cleavage damage in medium-grained sandstone results in a convoluted and intertwined crack path, consequently causing significant deformation.

4.4 Numerical simulation of the mechanical behavior of mesoscopic fractures

To clarify the mechanical behavior mechanism of fractures in tight sandstone, the internal mesoscopic structure is divided into three levels of grains, where level I is the rock itself, level II is the mineral crystal grains and level III is the aggregate of level II grains. A simplified tight sandstone model is shown in Fig. 13, where light gray represents quartz, which is the main component of tight sandstone; yellow represents feldspar; and dark grey represents clay minerals. According to the above mineral analysis results, a calcite content less than 2% weakly impacts the mechanical properties of the rock. The differences in the micromechanical properties of clay minerals and calcite are relatively small; therefore, calcite was not considered. In Fig. 13, the solid line represents the bonds between level III grains: the intragranular bond. The solid red line represents the internal bonds of quartz grains, the solid purple line represents the internal bonds of feldspar grains, and the solid blue line represents the internal bonds of clay minerals. The dotted lines represent the bonds between the level II grains: the intergranular bonds. The red dotted line represents the bond between quartz grains, the purple dotted line represents the bond between quartz grains and feldspar grains, and the blue dotted line represents the bond between quartz grains and clay minerals. When a tight sandstone sample is subjected to an external force, all types of bonds undergo tension or compression. Equations (13)–(15) show that the normal stiffness and tangential stiffness of the bond are positively proportional to the Young's modulus of the mineral and inversely proportional to the bond length (Cai et al. 2020). In addition, the length of the intragranular bond is less than that of the intergranular bond, resulting in increased stiffness of the intragranular bond and increased energy needed for fracture. In contrast, intergranular bonds are more likely to reach the fracture limit and generate microcracks than are intragranular bonds. Therefore, the initial cracks mostly develop between the crystals. The results of the targeted nanoindentation test show that the relationship of the Young's modulus of the minerals is as follows: $E_{\text{-quartz}} > E_{\text{-feldspar}} > E_{\text{-cement.}}$ Thus, in Fig. 13c, the relationship of the bond stiffnesses in different colors is as follows: red > purple > blue.

$$K_n = \frac{E}{L} \tag{13}$$

$$K_t = \frac{G}{L} \tag{14}$$

$$G = \frac{E}{2(1+\nu)} \tag{15}$$

where K_n and K_t are the normal stiffness and tangential stiffness of the bond, respectively; E and G are the Young's modulus and shear modulus of the minerals, respectively; and ν is the Poisson's ratio of the minerals (a small value has a negligible effect on the results).

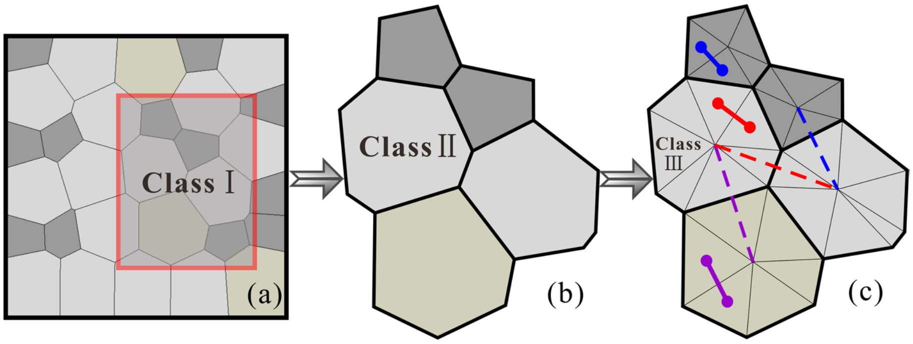

Fig. 13 Simplified model of tight sandstone

Tight sandstones with different grain sizes in the study area were investigated by conducting mesoscopic compression finite element simulation using the Voronoi polygon-based global cohesive model to visually characterize the rock damage mechanisms and fracture modes. The Voronoi polygon serves as a stochastic division of the two-dimensional plane, consisting of an assembly of contiguous polygons. These polygons are generated by the perpendicular bisectors of line segments that connect pairs of neighboring points. Because the grain size of fine-grained sandstone is between that of siltstone and medium-grained sandstone, the fracture style at the mesoscopic scale is not classic. In this study, models are developed based on siltstone and medium-grained sandstone with significant differences in grain size. Based on the grain size and mineral component distribution characteristics of the tight sandstone specimens and the results of the nanoindentation test, a 2 × 4 mm mesoscopic rock grain model was created using the Voronoi polygon mosaic principle. The grain size of the siltstone model was uniformly set to 0.05 mm. The grain sizes of the medium-grained sandstone model were unevenly distributed in the range of 0.24–0.34 mm. The Python program was used to insert cohesive elements with a thickness of 0 between the meshes of the model. The cohesive cell method operates on the principle of inserting zero-thickness grid nodes between two adjacent finite element meshes. This approach allows for the simulation of rock rupture processes by enabling the separation of these zero-thickness grid nodes, thereby permitting fractures to occur at any location. This overcomes the limitations of traditional cohesive models that require predefined fracture trajectories. Therefore, this model is relatively similar to the real rock fracture process. As shown in Fig. 14a, the light gray, yellow, and dark gray Voronoi polygons represent quartz, feldspar, and clay mineral grains, respectively, and the white line in the enlarged image represents the inserted cohesive elements. The mineral proportions and mineral grain sizes of the siltstone model and medium-grained sandstone model in this simulation were established according to the statistical results in Sect. 3.1 of this paper (Figs. 14b, c). The values of the mechanical parameters of each part of the model were determined by combining the results of the nanoindentation test in Sect. 3.2 of this paper with the parameter

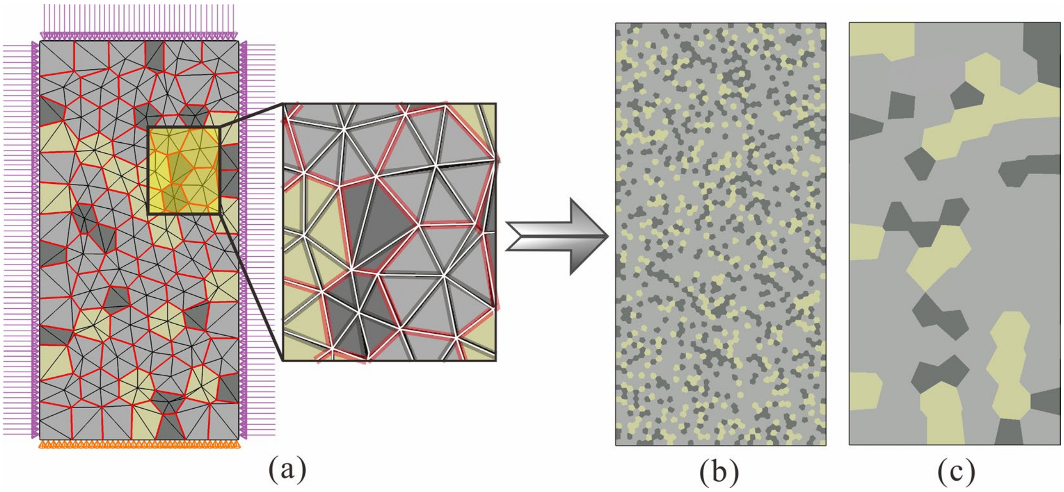

Fig. 14 **a** Schematic of the unified cohesive model based on Voronoi polygons; **b** Schematic of the siltstone model; **c** Schematic of the medium-grained sandstone model

Table 4 Basic composition and mineral information of tight sandstone models

Tight sandstone Species	Mineral Species	Mineral composition (%)	Number of grains	Young's modulus (MPa)	Poisson's ratio
Siltstone	Quartz	62	1984	90,000	0.17
	Feldspar	20	640	70,000	0.20
	Clay mineral	18	576	30,000	0.30
Medium-grained sandstone	Quartz	68	48	90,000	0.17
	Feldspar	20	16	70,000	0.20
	Clay mineral	12	17	30,000	0.30

Table 5 Mechanical parameters of the cohesive constitutive contact in the tight sandstone model

Cohesive	Elastic (MPa)			Max damage (MPa)		
	Enn	Ess	Ett	Nominal stress normal-only mode	Nominal stress first direction	Nominal stress second direction
Quartz	135	135	135	0.135	0.135	0.135
Feldspar	120	120	120	0.120	0.120	0.120
Clay mineral	45	45	45	0.045	0.045	0.045

assignment practices in previous studies (Wu et al. 2017; Wu et al. 2019; Wu et al. 2020). The specific assignments are shown in Tables 4 and 5.

The simulation results indicate that the initial cracks in both the siltstone and medium-grained sandstone models originated within the clay minerals located at the boundaries of the models. Furthermore, the axial displacements at the onset of crack formation and the ultimate axial displacements in the models were notably less than those observed in the medium-grained sandstone models (refer to Figs. 15a–d). The study involved

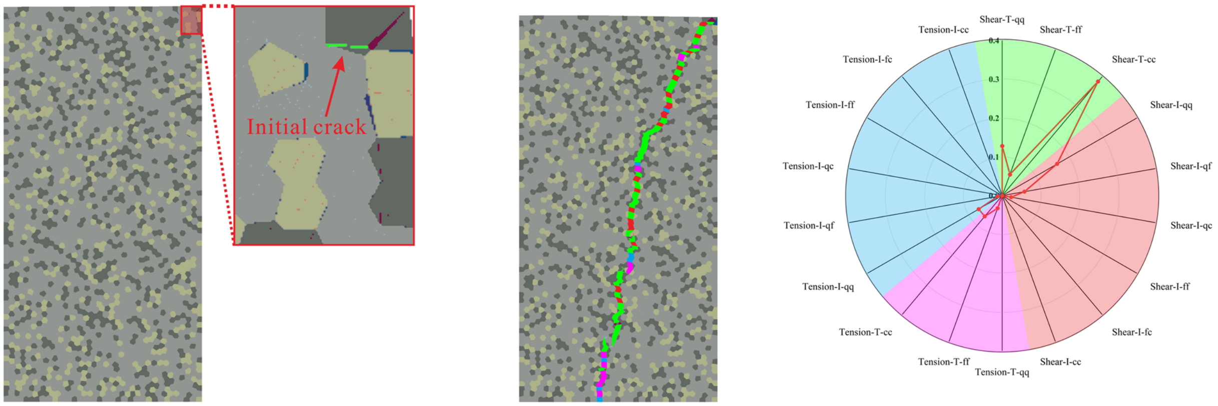

(a) step10;
displacement: 0.278E-03mm

(c) step100;
displacement: 0.0127mm

(e)

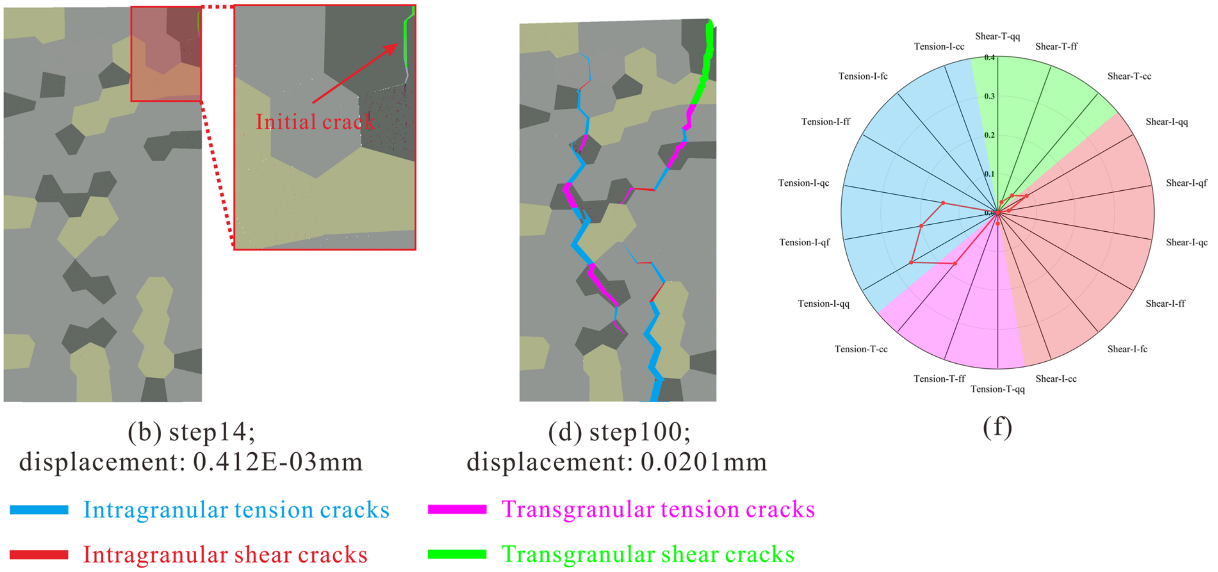

Fig. 15 **a** Simulation results of the siltstone model showing grain contours (initial crack); **b** Simulation results of the medium-grained sandstone model showing grain contours (initial crack); **c** Simulation results of the siltstone model showing grain contours (final state); **d** Simulation results of the medium-grained sandstone model showing grain contours (final state); **g** Statistics of different types of cracks in siltstone models; **h** Statistics of different types of cracks in medium-grained sandstone models

extracting and quantifying cracks in the simulation results. Statistical analysis revealed at the mesoscopic scale, cracks in siltstone with small average grain size and uniform distribution are primarily transgranular shear cracks, constituting 56.98% of the total crack population. Moreover, transgranular shear cracks with a single trajectory can coalesce along a consistent orientation to generate macroscopic straight shear cracks. The average grain size of large and unevenly distributed medium-grained sandstone primarily leads to the development of intergranular tension cracks, which account for 60% of the total number of cracks. The complexity and variability of the extension direction of these tension cracks facilitate effective communication between the cracks, thereby enabling the formation of a complex fracture network. This phenomenon accelerates the failure of the rock, resulting in a shorter strain localization phase in its stress–strain curve. The simulation results of siltstone and medium-grained sandstone share some common characteristics. Firstly, transgranular shear cracks in both predominantly occur in clay minerals. In the siltstone model, 67.35% of transgranular cracks are found in clay minerals, while in the medium-grained sandstone model, this percentage increases to 80%. Secondly, intergranular cracks in both models are primarily observed at the peripheries of quartz minerals. Notably, the highest proportion of intergranular cracks was observed between quartz and quartz (Figs. 15e, f). This phenomenon can be attributed to the relatively weaker resistance to deformation and higher fracture toughness of quartz, making it more prone to intergranular cracks due to stress concentration at its edges. In summary, the macromechanical behavior of tight sandstone is predominantly influenced by two critical factors. First, a smaller and more uniform mineral grain size promotes the development of transgranular shear cracks within the tight sandstone. Second, an elevated content of clay minerals and calcite with low fracture toughness enhances the likelihood of transgranular crack formation, which is macroscopically observed as single-shear fractures. Moreover, a higher concentration of quartz and feldspar is linked to a greater tendency for bending intergranular cracks, which are visually represented on a larger scale as stable brittle fractures.

The stress cloud map and displacement cloud map be utilized to visualize the non-uniform characteristics of stress distribution and mineral grain displacement during the compression process in the destruction of tight sandstone. The stress observed in the siltstone model a small average grain size and uniform distribution is primarily concentrated at model edges that were subjected to external forces. Only a few displacement anomalies are evident at the model edges and on both sides of the cracks. Overall, the stresses and displacements within the model' interior and unbroken areas exhibit a high level of homogeneity (see Figs. 16a, b). In contrast, the stress distribution in the medium-grained sandstone model a large average grain size and uneven distribution shows significant variation. Stress anomalies are present at both the model edges and inside the model, with displacement anomalies occurring in some unbroken areas as well as on both sides of the cracks. The number of stress-concentrated sites is numerous and irregularly distributed within the model interiors, leading to the early initiation of cracks and the development of more complex fracture patterns (see Figs. 16d, e). Additionally, the damage patterns identified through the simulations at the mesoscopic level closely matched the features of the macroscopic rupture patterns (Figs. 16c, f).

5 Discussion

5.1 Upscaling results and evaluation of microscale mechanical parameters

The results of 10 groups of micromechanical parameters were upscaled by the Mori–Tanaka two-phase homogenization method based on four components: quartz, feldspar, calcite, and clay minerals. The method takes into account the average matrix stress as well as the local stress fluctuation due to the dispersion of the secondary hardening phase in the primary matrix and is therefore well suited for composites with a low integral number of intercalated objects (Klusemann et al. 2011), while the volume fraction of inclusions (calcite and clay minerals) in the tight sandstone in the study area is also low (no more than 15% in most cases). The rock is homogenized in two steps. First, the clay minerals and pores in the tight sandstone are homogenized into a uniform clay pore medium that is equivalent to the two; second, the quartz, feldspar, calcite and uniform clay pore media are further homogenized as homogeneous rock material equivalent to the real tight sandstone (Fig. 17), and the specific calculation method is shown in the following equations (Mori and Tanaka 1973; Huang et al. 2014):

$$k_r = \frac{E_r}{3\left(1 - 2\nu_r\right)} \tag{16}$$

$$\mu_r = \frac{E_r}{2\left(1 + \nu_r\right)} \tag{17}$$

$$k_0 = \frac{4(1 - \varnothing)k_s\mu_s}{4\mu_s + 3\varnothing k_s} \tag{18}$$

$$\mu_0 = \frac{(1 - \varnothing)\mu_s}{1 + 6\varnothing\frac{k_s+2\mu_s}{9k_s+8\mu_s}} \tag{19}$$

$$k^{\mathrm{hom}} = \left(\sum_{r=0}^{3}\frac{f_r \times k_r}{3k_r + 4\mu_0}\right)\left(\sum_{r=0}^{3}\frac{f_r}{3k_r + 4\mu_0}\right)^{-1} \tag{20}$$

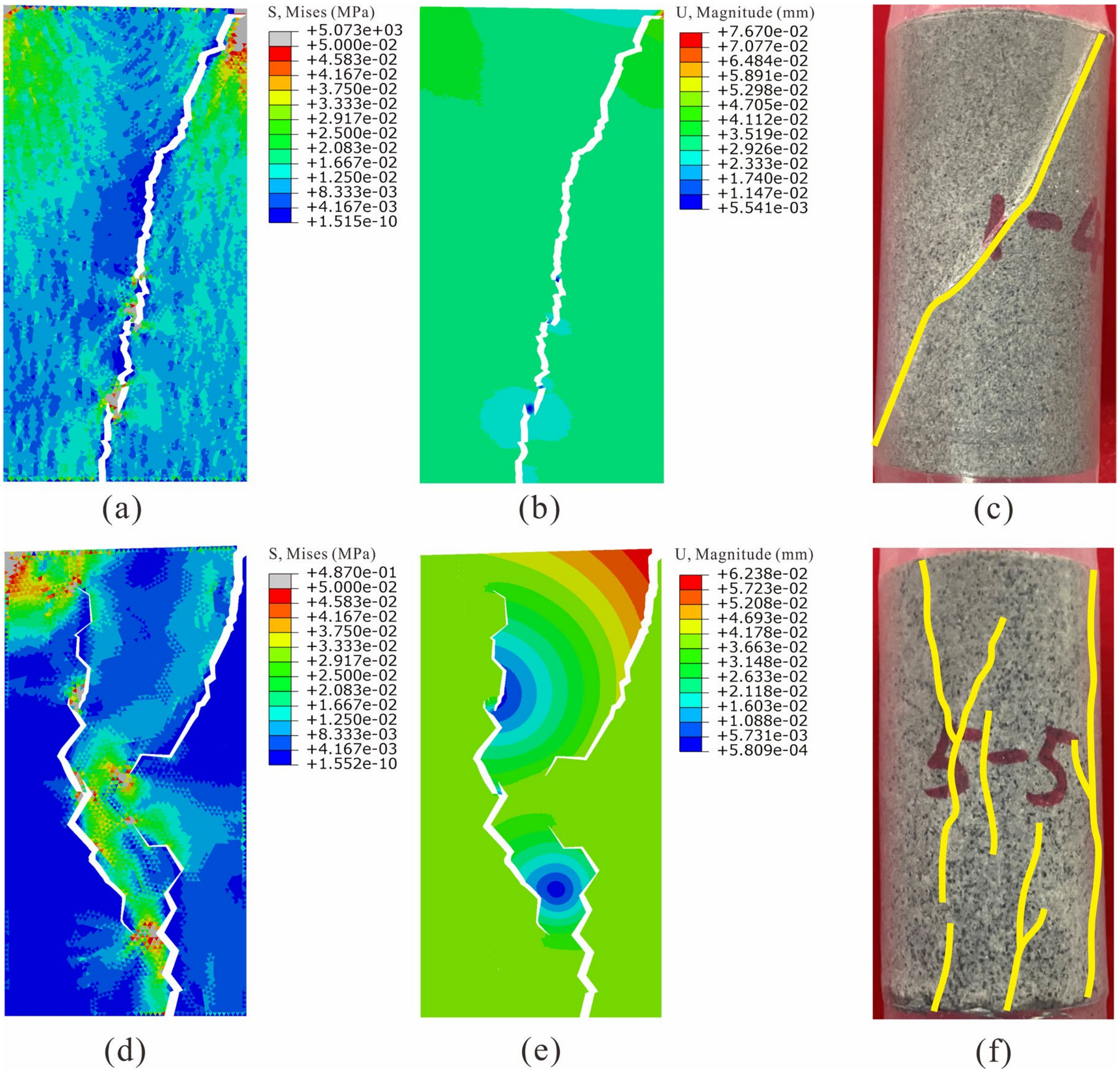

Fig. 16 **a** Distribution of stress values for the siltstone model; **b** Distribution of displacement values for the siltstone model; **c** Typical failure image of a siltstone sample after triaxial compression tests; **d** Distribution of stress values for the medium-grained sandstone model; **e** Distribution of displacement values for the medium-grained sandstone model; **f** Typical failure image of a medium-grained sandstone sample after triaxial compression tests

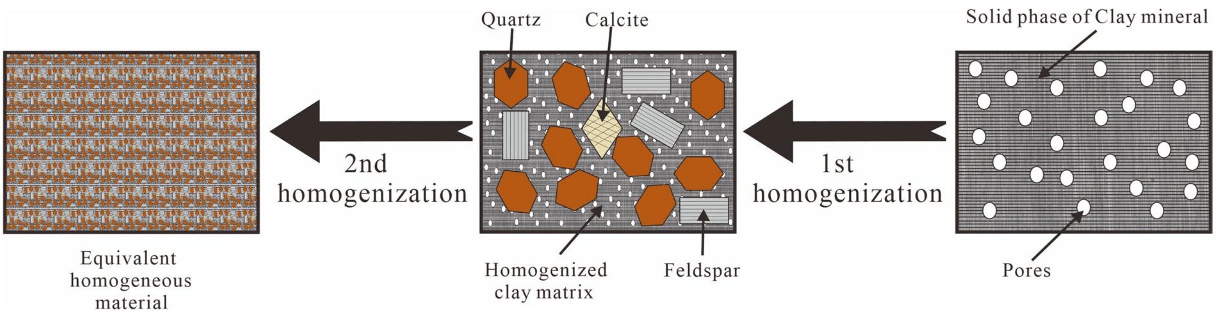

Fig. 17 Schematic of the two-step nonlinear homogenization procedure

$$G^{\mathrm{hom}} = \left(\sum_{r=0}^{3} \frac{f_r \times \mu_r}{\mu_0\left(9k_0 + 8\mu_0\right) + 6\mu_r\left(k_0 + 2\mu_0\right)}\right)\left(\sum_{r=0}^{3} \frac{f_r}{\mu_0\left(9k_0 + 8\mu_0\right) + 6\mu_r\left(k_0 + 2\mu_0\right)}\right)^{-1} \tag{21}$$

where k_r and μ_r ($r = 1,2,3$) respectively denote the volume modulus and shear modulus of quartz, feldspar, and calcite (these three types of minerals can be approximated as elastically tight and homogeneous materials); E_r and ν_r ($r = 1,2,3$) respectively denote Young's modulus and Poisson's ratio of quartz, feldspar, and calcite (since the Poisson's ratio of similar minerals does not vary much, the Poisson's ratio for quartz is taken as 0.15, that of feldspar is taken as 0.2, and that of calcite is taken as 0.25); k_0 and μ_0 respectively denote the volume modulus and shear modulus of the homogenized clay matrix; k_s and μ_s respectively denote the volume modulus and shear modulus of the solid phase of the clay mineral; Φ is the porosity of the clay mineral, with an empirical value of 3.5%; and f_r ($r = 0,1,2,3$) denotes the volumetric fraction of the clay minerals, quartz, feldspar, and calcite.

The results of two-phase homogenization upscaling are shown in Fig. 18. The results for the upscaled Young's modulus are generally greater than the measured values from the triaxial compression test. This result arises because local damage (microcracks) may occur in the macroscale core, and during the triaxial compression process, due to the weak microcracks, stress concentration is likely to occur and develop into macroscopic fractures, reducing the macroscopic mechanical parameters of the rock (Charlton et al. 2021). The relative error coefficient [$\delta = $(Young's modulus after scaling up − actual Young's modulus)/actual Young's modulus] is introduced to evaluate the upscale results of tight sandstone in the study area. The results show that for the 10 groups of scaled-up Young's moduli in the study area, the relative deviations and the measured values obtained from the triaxial compression test are in the range of 47.4%–108.5%. After excluding the maximum and minimum values of the relative deviation coefficient, the scaled-up results and measured values are strongly correlated. A positive correlation ($R^2 = 0.91$) indicates that the values of the relative rock mechanical parameters before and after scaling up are very consistent. The observed greater divergence from the trend line in two specific samples can be attributed to substantial variations in their internal microstructure, which significantly deviate from those of the other samples. In summary, this upscaling method is suitable for tight sandstone, and it can be used to quickly calculate the macromechanical properties of intact rocks of arbitrary shapes using nanoindentation results.

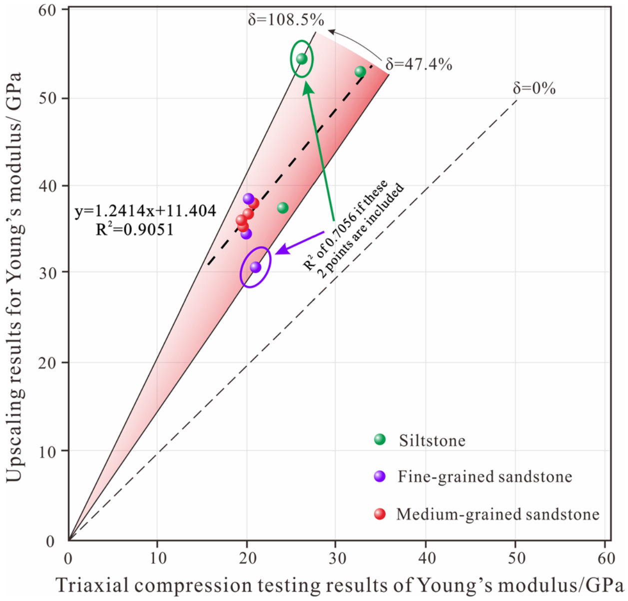

Fig. 18 Young's modulus upscaling results for 10 groups of tight sandstone specimens

5.2 Effects of multiscale mechanical properties and fracture mechanical behaviors

According to the Hall−Petch (H–P) relationship, the effects of grain size on the mechanical properties of a material can be determined via Eq. (22) (Ma et al. 2021):

$$\mathrm{H(d)} = H_0 + kd^{-1/2} \tag{22}$$

where H(d) is the hardness of the polycrystalline material, H_0 is the hardness of a single grain, k is a material constant, and d is the mean grain size.

According to the above equation, the yield strength of the material increases with decreasing grain size, which is consistent with the results of the triaxial test: $E_{\text{siltstone}} > E_{\text{fine-grained sandstone}} > E_{\text{medium-grained sandstone}}$. However, the H–P relationship can characterize only the relationships among the magnitudes of rock mechanical parameters and cannot explain the micromechanical processes of crystalline rocks.

The micromechanical fracture process of tight sandstone specimens with different grain sizes was also analyzed. According to the average grain microstrain formula and mesoscopic numerical simulation results (Eq. (23)) (Hu 2022), under the same deformation amount, for siltstone specimens with small and uniform grain sizes, $Q_{k_s k_{s+1}}$ is closer to 1, and the external normal vectors ($b_{k_s k_{s+1}}$) between each group

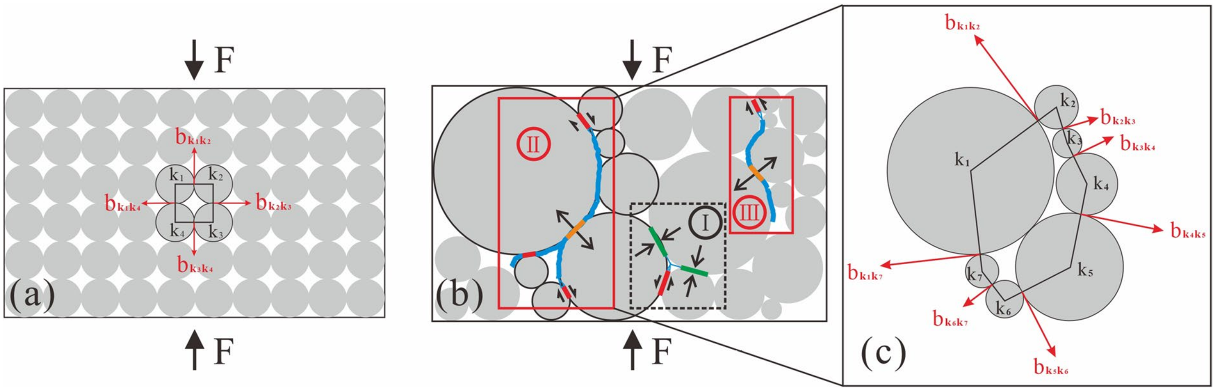

Fig. 19 Schematic of microscopic fracture in tight sandstone. **a** Schematic of microstrain in tight sandstone with small and uniform grain sizes; **b** Schematic of the fracture process in tight sandstone with large and nonuniform grain sizes; **c** Schematic of microstrain in tight sandstone with large and nonuniform grain sizes

of grains are approximately the same. Therefore, there is almost no difference in the relative displacement between each group of grains, and the deformation is more evenly distributed in additional grains, reducing the tendency of stress concentration at the grain boundaries and cracking. Therefore, the smaller the grain size of the sample is, the greater the strength (Fig. 19a). In addition, as a result, additional grain boundaries accumulate within a certain volume, the shearing and rotation resistance at the grain boundaries increase, and dislocation slip is easily hindered at the grain boundaries, thus decreasing the gap between the grain boundaries and the ultimate strength of the intragranular fracture. Therefore, inhibiting the propagation of many intergranular cracks (Li et al. 2021c) and manifesting macroscopically as straight cracks with large angles.

$$\overline{a_T} = \frac{1}{L}\left(\sum_{s=1}^{L} Q_{k_sk_{s+1}} \Delta\mu_{k_sk_{s+1}} b_{k_sk_{s+1}}\right) \tag{23}$$

where $\overline{a}_T$ is the average microstructural strain of the grain; $Q_{k_sk_{s+1}}$ is the difference in grain size between grains; $\Delta\mu_{k_sk_{s+1}}$ is the relative displacement between grains; $b_{k_sk_{s+1}}$ is the external normal vector of two grains, with a magnitude equal to the sum of the radii of the two grains; and L is the quantity of grains contained in the grain.

As the grain size of the fine and medium-grained sandstone increases, the uniformity of the grain size decreases, weak spots such as gaps and microcracks are more likely to exist between grains, and the grain boundary bonding strength decreases. As shown in Fig. 19b, there are grains of different sizes, and there are large differences in the Q $_{\mathrm{ksks+1}}$ of each group; as a result, a locally uneven stress distribution is prone to occur. Figure 19c shows that the k_1k_7 grain group with the largest difference in grain size has the largest $b_{\mathrm{ksks+1}}$; therefore, the deformation of the k_1k_7 group is the largest. With a constant global deformation, stress concentration can occur between the k_1k_7 groups. In addition, since the grains at the edge of the sample are in the slip state, they are more likely to rotate and lead to failure; thus, the stress concentration first appears at the position of the red line in Fig. 19b. As the stress continues to increase, open cracks appear in the stress concentration area. Due to the higher and uneven distribution of stress concentration in medium-grained sandstone compared to siltstone, the former exhibits a lower crack initiation stress. Additionally, the presence of more voids in medium-grained sandstone allows for greater deformation space, resulting in a higher crack initiation strain compared to siltstone. If there are stronger compression grain boundaries (green line) on both sides and if the direction of the opening crack is facing the grains, only the stress concentration area accumulates energy. When the stress concentration area is high enough and the intermediate grain strength is low enough, transgranular cracks form, but this crack formation process is relatively difficult (Fig. 19b, region I). The mesoscopic numerical simulation findings indicate that merely 28.57% of the transgranular cracks occur in the medium-grained sandstone, while 80% of the transgranular cracks are located within the clay minerals exhibiting the lowest fracture toughness. If the stress concentration location gradually extends along the opening direction to the lower strength tension grain boundary (orange line), the energy is unloaded, and the cracking energy needed inside the crystal cannot be achieved. Thus, the grains are avoided, and propagation occurs around the core, gradually developing into intergranular cracks at a certain scale (regions II and III in Fig. 19b). This is the cause of the highest percentage (60%) of intergranular tension cracks developed in the medium-grained sandstone. Intergranular cracks predominantly developed in medium-grained sandstone, in contrast to the formation of transgranular cracks in the siltstone. Compared to transgranular cracks, intergranular cracks are initiated at lower stress. The displacement variables resulting from intergranular tension cracks are notably larger than those from the other three types of cracks. Therefore, medium-grained sandstone exhibit lower crack damage stress and peak stress compared to siltstone, but they demonstrate higher crack damage strain and peak strain. And intergranular cracks require less energy and their complex path characteristics make it easier to connect with other microcracks, leading to a significant increase in crack propagation rate, surpassing the critical speed and resulting in instability, and a more extensive and multidimensional damage area. It is precisely why medium-grained sandstone has a lower macroscopic Young's modulus. Therefore, compared to the content of hard minerals such as quartz, the microstructure of rock has a greater influence on the overall mechanical properties and fracture behavior. When evaluating the stability and sealing of CO_2 sequestration sites, siltstone, which has a more uniform microstructure, is clearly the optimal choice for caprock.

5.3 Application to the effect of variable failure characteristics of tight sandstone on CO_2 sequestration capacity

To evaluate the impact of macro–micro fracture characteristic variability in different tight sandstone roofs of coal seams on CO_2 sequestration capacity, stress sensitivity experiments were conducted on representative samples of medium-grained sandstone and siltstone following triaxial compression experiments. Subsequently, 3D laser scanning of the fracture surfaces was performed, and the dataset comprising 3D coordinates of fracture surface morphology was imported into Surfer software for the initial reconstruction of fracture surface morphology (Figs. 20a, b). The findings indicate that the overall height of the split fracture surface and the non-uniformity of its distribution resulting from the medium-grained sandstone samples (with mean and root mean values of the fracture surface height being $h_C = 4.302 \pm 0.819$ mm and $h_{RMS} = 4.379$ mm, respectively) were notably higher compared to the shear fracture observed in the siltstone ($h_C = 3.024 \pm 0.826$ mm and $h_{RMS} = 3.135$ mm). In other words, the roughness of the

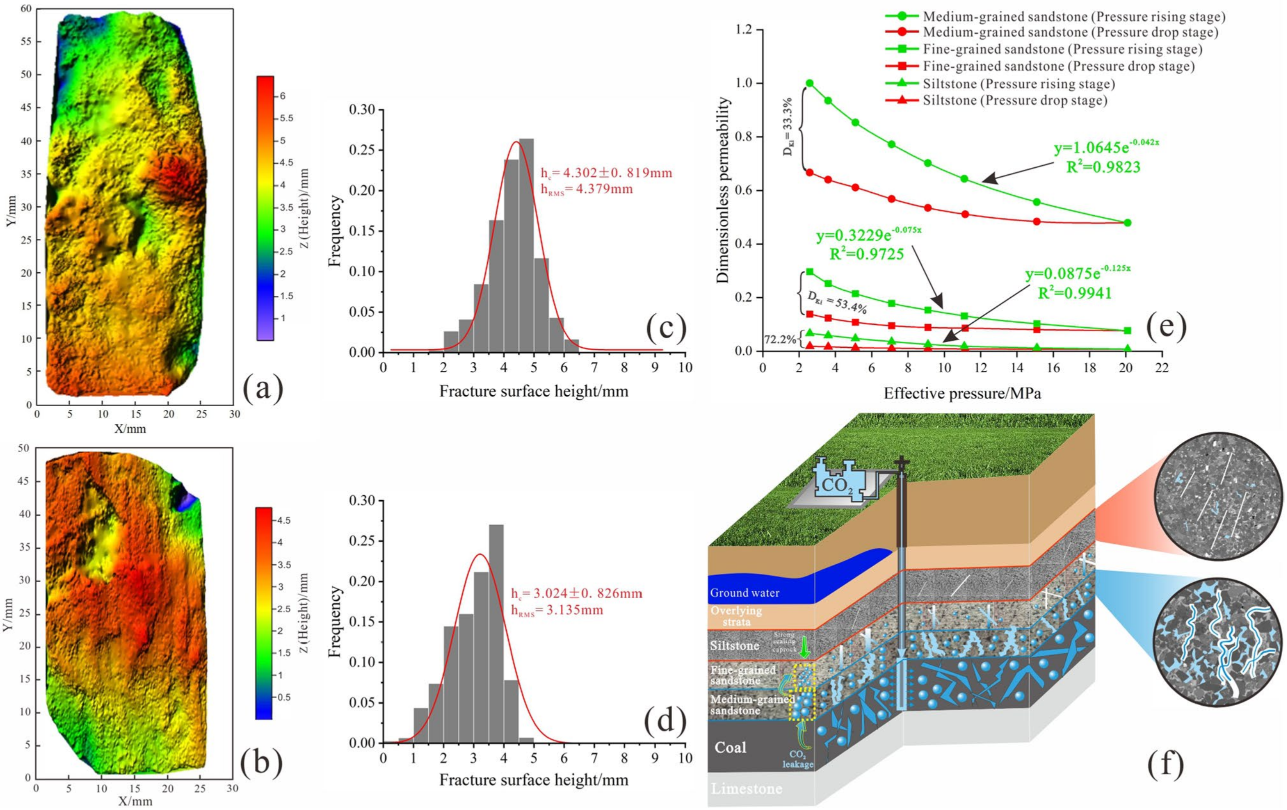

Fig. 20 **a** 3D laser scanning view of the fracture surface of medium-grained sandstone sample; **b** 3D laser scanning view of the fracture surface of siltstone sample; **c** Histogram of the height distribution of the fracture surface of medium-grained sandstone sample; **d** Histogram of the height distribution of the fracture surface of siltstone sample; **e** Experimental curves of stress-sensitive flow for various types of sandstone; **f** Map of CO_2 sequestration patterns in the tight sandstone formation

fracture surface created by the medium-grained sandstone is significantly higher (Figs. 20c, d). The experimental results indicate a decrease in the permeability of different types of tight sandstone samples as the confining pressure increases. The relationship between permeability and confining pressure follows a negative exponential function, with a fitting degree exceeding 96% (Fig. 20e). The relationship equation is expressed as:

$$K_{\mathrm{i}} = K_0 e^{-K_\varphi P_{\mathrm{i}}} \tag{24}$$

where K_{i} represents the permeability under a specific pressure condition, mD; P_{i} denotes the effective stress ranging from the initial to a specific pressure condition, MPa; K_0 stands for the permeability at zero initial pressure, mD; and K_φ indicates the permeability stress sensitivity factor, MPa^{-1}.

The results of the stress sensitivity experiments indicate that the overall permeability of the medium-grained sandstone samples is notably higher compared to the fine-grained sandstone and siltstone samples. Additionally, the stress sensitivity coefficient ($K_\varphi = 0.042\ \mathrm{MPa}^{-1}$) and irreversible permeability damage rate ($D_{\mathrm{Ki}} = 33.3\%$) of the medium-grained sandstone samples are significantly lower than those of the fine-grained sandstone samples ($K_\varphi = 0.075\ \mathrm{MPa}^{-1}$; $D_{\mathrm{Ki}} = 53.4\%$) and the siltstone samples ($K_\varphi = 0.125\ \mathrm{MPa}^{-1}$; $D_{\mathrm{Ki}} = 72.2\%$). The findings suggest that the medium-grained sandstone exhibits a higher seepage capacity in comparison to the siltstone and fine-grained sandstone under identical stress conditions. This observation can be linked to the high roughness of fracture surfaces formed in the medium-grained sandstone specimens. The increased roughness enhances the internal spatial complexity and the quantity of flow channels within the samples. Additionally, the presence of numerous intergranular cracks may contribute to mineral dislodgement, consequently augmenting the support points on the fracture surfaces. The low stress sensitivity and high permeability resulting from the macro–micro fracture characteristics of the medium-grained sandstone enable efficient absorption of leaked CO_2 from the coal seam, providing a robust long-term sequestration capacity. Fine-grained sandstone exhibits moderate permeability and stress sensitivity. Owing to the positive rhythm depositional attributes of the target layer within the research area, the fine-grained sandstone can serve as a transitional zone for CO_2 sequestration between the medium-grained sandstone and the siltstone. This zone captures a fraction of the CO_2 and diminishes the upward diffusion capacity of CO_2, thereby preventing it from reaching the breakthrough pressure of the siltstone caprock. The high-stress sensitivity and low permeability of siltstone offer significant advantages in minimizing the risk of CO_2 leakage, making it a suitable candidate for serving as a high-quality caprock in CO_2 sequestration applications. The utilization of medium-grained sandstone as a substrate for absorbing CO_2 leakage from coal seams, combined with siltstone as a sealing caprock, can enhance the effectiveness of CO_2 sequestration in deep, unmineable coal seams. (refer to Fig. 20f).

6 Conclusions

(1) The micromechanical strength of minerals in the tight sandstones exhibit the order of quartz > feldspar > calcite > clay minerals. The mechanical properties of monocrystalline quartz are significantly stronger than those of polycrystalline quartz. Minerals with stronger mechanical properties have more stable microstructures, smoother *P–h* curves, and lower dispersions of micromechanical parameters, which leads to small fractures. Minerals with weak micromechanical properties are likely to generate shear cracks caused by plastic deformation in triangular dents, which can develop into lateral cracks and surface spalling.

(2) Among different tight sandstone types, siltstone exhibits the most robust macro-mechanical properties, characterized by Young's modulus and Poisson's ratio values of 28.52 ± 5.67 GPa and 0.163 ± 0.050, respectively. This is followed by fine-grained sandstone and medium-grained sandstone. As the mineral particle size and non-uniformity increase, the elastic stage of tight sandstone shortens, leading to earlier crack initiation and propagation. Consequently, the fracture pattern tends to exhibit complex longitudinal splitting damage.

(3) After scaling up the two-phase homogenization process, in most cases, Young's modulus is lower than that of the triaxial test result. This difference arises because the two-phase homogenization scale-up method does not consider the local damage that exists in the core at the macroscopic scale. However, there is a strong correlation between the two ($R^2 = 0.91$), indicating that the upscaled results can effectively reflect the relative rock mechanical properties of tight sandstone. This method can be used to rapidly evaluate the mechanical properties of tight sandstone specimens in various deep earth engineering applications.

(4) The larger the grain size, the greater the number of weak spots, such as gaps, between the grains and the lower the fracture strength at the grain boundary. In addition, the larger the grain size, the more scattered the grain size distribution and the more prone the grains are to stress concentration. Due to low strength at grain boundaries, there is little energy accumulation between grains, and unloading occurs easily at weak spots, with the result being that the energy level is insufficient to penetrate the grains. Thus, more intergranular cracks

are generated, which also leads to a greater degree of macroscopic failure. This low energy accumulation leads to the weak macromechanical properties of the fine and medium-grained sandstone. The combination of weak plasticity and high fracture toughness in quartz facilitates stress concentration at its edges, making intergranular cracks more likely to form. Conversely, the strong plasticity and low fracture toughness of clay minerals make them prone to being cut through easily, resulting in transgranular cracks predominantly within the clay minerals.

(5) The split damage generated by medium-grained sandstone exhibits weak stress sensitivity and high permeability, making it the most suitable coal seam roof for continued CO_2 sequestration. Conversely, siltstone demonstrates robust macro-mechanical properties, with shear damage showing high-stress sensitivity and low permeability—this characteristic grants siltstone effective closure and stability when employed as a caprock.

Acknowledgements This work was supported by the project from the Exploration and Development Research Institute of PetroChina Daqing Oilfield Company. The authors greatly acknowledge the financial support from the research by the National Natural Science Foundation of China (42402148), Sichuan Provincial Fund (24NSFSC4997), and Guizhou Outstanding Young Science and Technology Talent Program (YQK[2023]012).

Author's contribution FC: Writing-Original draft preparation, Writing-Reviewing and Editing, Methodology, and Investigation. JH: Conceptualization, Methodology, Investigation, Supervision. HC: Writing-Original draft preparation. HD: Supervision, Methodology. ADLC: Writing-Reviewing and Editing. RJ: Writing-Original draft preparation. RL: Writing-Reviewing and Editing. JL: Writing-Original draft preparation.

Declarations

Competing interests We declare that we have no financial and personal relationships with other people or organizations that can inappropriately influence our work, there is no professional or other personal interest of any nature or kind in any product, service and/or company that could be construed as influencing the position presented in, or the review of the manuscript 'Quantitative characterization of the multi-scale mechanical properties of low-permeability sandstone roofs of coal seams based on nanoindentation and triaxial tests and its implications for CO_2 geological sequestration'.

References

Abdallah Y, Vandamme M, Chateau C et al (2023) Linking elastic properties of various carbonate rocks to their microstructure by coupling nanoindentation and SEM-eds. Int J Rock Mech Min Sci 170:105456

Abedi S, Slim M, Hofmann R et al (2016) Nanochemo-mechanical signature of organic-rich shales: a coupled indentation–EDX analysis. Acta Geotech 11:559–572

Abou-Chakra Guéry A, Cormery F, Shao J-F, Kondo D (2010) A comparative micromechanical analysis of the effective properties of a geomaterial: effect of mineralogical compositions. Comput Geotech 37:585–593

Bobko C, Ulm F-J (2008) The nano-mechanical morphology of Shale. Mech Mater 40:318–337

Cai P, Xuan W, Zhang T et al (2020) Investigation into the crushing process in multi-scale cohesive particle model. Rock Soil Mech 41:1809–1817

Charlton TS, Goodarzi M, Rouainia M et al (2021) Effect of diagenesis on geomechanical properties of organic-rich calcareous shale: a multiscale investigation. J Geophys Res Solid Earth 214:21365

Cheng Y-T, Li Z, Cheng C-M (2002) Scaling relationships for indentation measurements. Philos Mag A 82:1821–1829

Cheng P, Zhang CP, Ma ZY et al (2022) Experimental study of micromechanical properties alterations of shale matrix treated by $SCCO_2$-water saturation using nanoindentation tests. Energy 242:122965

Cong R, Yang R, Li G et al (2023) Geomechanical properties of thinly interbedded rocks based on micro- and macro-scale measurements. Rock Mech Rock Eng 56:5657–5675

Donnelly E, Baker SP, Boskey AL, van der Meulen MCH (2006) Effects of surface roughness and maximum load on the mechanical properties of cancellous bone measured by nanoindentation. J Biomed Mater Res Part A 77A:426–435

Du J, Whittle AJ, Hu L et al (2020) Characterization of meso-scale mechanical properties of Longmaxi Shale using grid microindentation experiments. J Rock Mech Geotech Eng 13:555–567

Gale J, Freund P (2001) Coal-bed methane enhancement with CO_2 sequestration worldwide potential. Environ Geosci 8:210–217

Guo Y, Chi SC, Mi XF (2021) Experimental study on particle strength and elastic mechanical parameters of coarse-grained soil. Chin J Geotech Eng 43(09):1675–1681

Gupta I, Sondergeld C, Rai C (2020) Fracture toughness in shales using nano-indentation. J Petrol Sci Eng 191:107222

Hu HR (2022) Research on the deformation and failure mechanism of sandstone based on macro-meso-micro scale. Chongqing University, pp .87–92

Hu C, Li Z (2015) A review on the mechanical properties of cement-based materials measured by nanoindentation. Constr Build Mater 90:80–90

Huang Y, Shen WQ, Shao JF et al (2014) Multi-scale modeling of time-dependent behavior of claystones with a viscoplastic compressible porous matrix. Mech Mater 79:25–34

Huang X, Qi S, Guo S et al (2022) Effect of the crystal habit on micromechanical extensile behaviors of the crystalline rock during compression. Eng Geol 310:106874

Jia CJ, Xu WY, Wang RB et al (2018) Experimental investigation on shear creep properties of undisturbed rock discontinuity in Baihetan Hydropower Station. Int J Rock Mech Min Sci 104:27–33

Klusemann B, Denzer R, Svendsen B (2011) Microstructure-based modeling of residual stresses in WC-12CO-sprayed coatings. J Therm Spray Technol 21:96–107

Kneuker T, Hammer J, Shao H et al (2017) Microstructure and composition of brittle faults in claystones of the Mont Terri Rock Laboratory (Switzerland): new data from petrographic studies, geophysical borehole logging and permeability tests. Eng Geol 231:139–156

Kossovich EL, Dobryakova NN, Epshtein SA, Belov DS (2016) Mechanical properties of coal microcomponents under continuous indentation. J Min Sci 52:906–912

Li C, Wang D, Kong L (2021a) Mechanical response of the Middle Bakken rocks under triaxial compressive test and nanoindentation. Int J Rock Mech Min Sci 139:104660

Li XF, Li HB, Zhao J (2021b) Transgranular fracturing of crystalline rocks and its influence on rock strengths: Insights from a grain-scale continuum–discontinuum approach. Comput Methods Appl Mech Eng 373:113462

Li Y, Luo S, Lu M et al (2021c) Cross-scale characterization of sandstones via statistical nanoindentation: evaluation of data analytics and upscaling models. Int J Rock Mech Min Sci 142:104738

Li J, Zhang M, Wang C et al (2024) Failure characteristics and fracture mechanism of overburden rock induced by mining: a case study in China. Int J Coal Sci Technol 11:44

Liang K, Xie L, He B et al (2021) Effects of grain size distributions on the macro-mechanical behavior of rock salt using micro-based multiscale methods. Int J Rock Mech Min Sci 138:104592

Liu W, Yang K, Zhang S et al (2022) Energy evolution and water immersion-induced weakening in sandstone roof of coal mines. Int J Coal Sci Technol 9:53

Luo S, Lu Y, Wu Y et al (2020) Cross-scale characterization of the elasticity of shales: statistical nanoindentation and data analytics. J Mech Phys Solids 140:103945

Ma Z, Pathegama Gamage R, Zhang C (2020) Application of nanoindentation technology in rocks: a Review. Geomech Geophys Geo-Energy Geo-Resour 6:60

Ma Z, Pathegama Gamage R, Zhang C (2021) Effects of temperature and grain size on the mechanical properties of polycrystalline quartz. Comput Mater Sci 188:110138

Ma Z, Zhang C, Pathegama Gamage R, Zhang G (2022) Uncovering the creep deformation mechanism of rock-forming minerals using nanoindentation. Int J Min Sci Technol 32:283–294

Magnenet V, Auvray C, Francius G, Giraud A (2011) Determination of the matrix indentation modulus of Meuse/Haute-Marne argillite. Appl Clay Sci 52:266–269

Manjunath GL, Jha B (2019) Nanoscale fracture mechanics of gondwana coal. Int J Coal Geol 204:102–112

Meng F, Wong LN, Zhou H, Wang Z (2018) Comparative study on dynamic shear behavior and failure mechanism of two types of granite joint. Eng Geol 245:356–369

Mori T, Tanaka K (1973) Average stress in matrix and average elastic energy of materials with misfitting inclusions. Acta Metall 21:571–574

Nie B, He H, Liu P et al (2024) Nanomechanical behavior of coal with heterogeneous minerals and pores using nanoindentation. Environ Sci Pollut Res 31:28007–28024

Ohmura T, Wakeda M (2021) Pop-in phenomenon as a fundamental plasticity probed by nanoindentation technique. Materials 14:1879

Oliver WC, Pharr GM (1992) An improved technique for determining hardness and elastic modulus using load and displacement sensing indentation experiments. J Mater Res 7:1564–1583

Pan Z, Ye J, Zhou F et al (2017) CO_2 storage in coal to enhance coalbed methane recovery: a review of field experiments in China. Int Geol Rev 60:754–776

Rutqvist J, Birkholzer JT, Tsang C-F (2008) Coupled reservoir–geomechanical analysis of the potential for tensile and shear failure associated with CO_2 injection in multilayered reservoir–caprock systems. Int J Rock Mech Min Sci 45:132–143

Sone H, Zoback MD (2014) Time-dependent deformation of shale gas reservoir rocks and its long-term effect on the in situ state of stress. Int J Rock Mech Min Sci 69:120–132

Spangenberg E (1998) A fractal model for physical properties of porous rock: theoretical formulations and application to elastic properties. J Geophys Res Solid Earth 103:12269–12289

Sun C, Li G, Elgharib Gomah M et al (2020a) Meso-scale mechanical properties of mudstone investigated by nanoindentation. Eng Fract Mech 238:107245

Sun C, Li G, Gomah ME et al (2020b) Creep characteristics of coal and rock investigated by nanoindentation. Int J Min Sci Technol 30:769–776

Sun C, Li G, Xu J et al (2021) Rheological characteristics of mineral components in sandstone based on nanoindentation. Chin J Rock Mech Eng 40:77–87

Tang X, Xu J, Zhang Y et al (2022) The rock-forming minerals and macroscale mechanical properties of asteroid rocks. Eng Geol 321:107154

Wu Z, Fan L, Liu Q, Ma G (2017) Micro-mechanical modeling of the macro-mechanical response and fracture behavior of rock using the numerical manifold method. Eng Geol 225:49–60

Wu Z, Sun H, Wong LN (2019) A cohesive element-based numerical manifold method for hydraulic fracturing modelling with Voronoi grains. Rock Mech Rock Eng 52:2335–2359

Wu Z, Ji X, Liu Q, Fan L (2020) Study of microstructure effect on the nonlinear mechanical behavior and failure process of rock using an image-based-FDEM model. Comput Geotech 121:103480

Xing Y, Xu X, Gui X et al (2017) Effect of kaolinite and montmorillonite on fine coal flotation. Fuel 195:284–289

Xu D, Liu X, Xu H et al (2021) Meso-mechanical properties of deep granite using nanoindentation test and homogenization approach. J Cent South Univ 52:2761–2771

Zhang K, Sang S, Zhou X et al (2021) Influence of Supercritical CO_2-H_2O-caprock interactions on the sealing capability of deep coal seam caprocks related to CO_2 geological storage: a case study of the silty mudstone caprock of coal seam no. 3 in the Qinshui Basin, China. Int J Greenh Gas Control 106:103282

Zheng S, Yong R, Du SG et al (2023) Relationship between macro and micro friction coefficients of sandstone structural surface based on nano-scratch test. Rock Soil Mech 44:1022–1034

Zhou X, Sang S, Niu Q et al (2021) Changes of multiscale surface morphology and pore structure of mudstone associated with supercritical CO_2-water exposure at different times. Energy Fuels 35:4212–4223